Dynamics of Atmospheres and Oceans
35 (2002) 97–130

dynamics
of atmospheres
and oceans

www.elsevier.com/locate/dynatmoce

Wind driven general circulation of the Mediterranean Sea simulated with a Spectral Element Ocean Model

A. Molcard [a,c], N. Pinardi [b,*], M. Iskandarani [c], D.B. Haidvogel [d]

[a] *Institute of Physical Oceanography-CNR, Lerici, La Spezia, Italy*
[b] *Department of Physics, Viale Berti Pichat, Bologna, Italy*
[c] *RSMAS/MPO, University of Miami, Miami, FL, USA*
[d] *Institute of Marine and Coastal Sciences, Rutgers University, New Brunswick, NJ, USA*

Received 13 July 2000; accepted 20 June 2001

Abstract

This work is an attempt to simulate the Mediterranean Sea general circulation with a Spectral Finite Element Model. This numerical technique associates the geometrical flexibility of the finite elements for the proper coastline definition with the precision offered by spectral methods. The model is reduced gravity and we study the wind-driven ocean response in order to explain the large scale sub-basin gyres and their variability. The study period goes from January 1987 to December 1993 and two forcing data sets are used. The effect of wind variability in space and time is analyzed and the relationship between wind stress curl and ocean response is stressed. Some of the main permanent structures of the general circulation (Gulf of Lions cyclonic gyre, Rhodes gyre, Gulf of Syrte anticylone) are shown to be induced by permanent wind stress curl structures. The magnitude and spatial variability of the wind is important in determining the appearance or disappearance of some gyres (Tyrrhenian anticyclonic gyre, Balearic anticyclonic gyre, Ionian cyclonic gyre). An EOF analysis of the seasonal variability indicates that the weakening and strengthening of the Levantine basin boundary currents is a major component of the seasonal cycle in the basin.

The important discovery is that seasonal and interannual variability peak at the same spatial scales in the ocean response and that the interannual variability includes the change in amplitude and phase of the seasonal cycle in the sub-basin scale gyres and boundary currents. The Coriolis term in the vorticity balance seems to be responsible for the weakening of anticyclonic structures and their total disappearance when they are close to a boundary.

The process of adjustment to winds produces a train of coastally trapped gravity waves which travel around the eastern and western basins, respectively in approximately 6 months.

* Corresponding author. Present address: University of Bologna, Corso di Laurea in Scienze Amb., Piazza J.F. Kennedy, no. 12, Palazzo Rasponi, 48100 Ravenna, Italy. Tel.: +39-544-484269; fax: +39-544-484268.
E-mail addresses: molcard@iof.cnr.it (A. Molcard), n.pinardi@ambra.unibo.it (N. Pinardi).

PII: S0377-0265(01)00080-X

This corresponds to a phase velocity for the wave of about 1 m/s, comparable to an average velocity of an internal Kelvin wave in the area.

Keywords: Numerical modelling; Interannual and seasonal variability; Empirical orthogonal functions

1. Introduction

The combination of several observational programs with model simulations allows the understanding of the Mediterranean Sea general circulation processes and variability. The general circulation structure of the Mediterranean Sea has been described in detail in many papers, such as Robinson and Golnaraghi (1993), Malanotte-Rizzoli et al. (1998), Roussenov et al. (1995), and Millot (1994). Here we will only say that the general circulation is now thought to be composed of sub-basin scale gyres, boundary currents and free jets. Robinson et al. (1991) pioneered the definition of the eastern Mediterranean circulation in terms of sub-basin scale gyres and jets in contrast with the traditional picture of a smooth cyclonic flow encircling the whole Mediterranean Sea basin. The existence of such gyres and currents was almost unknown in the middle 1980s and the observational programs of the last decade, together with the numerical modeling, have helped to clarify the structure and variability of the circulation. However, the relative importance of general circulation forcings (momentum, heat, salt) on these structures is still under question as well as the role of internal variability due to the mesoscale. In this paper we attempt a process-oriented study of the wind-driven circulation trying to highlight the connections between wind stress structures and the ocean response and the processes associated with adjustment to winds.

The importance of the wind and wind stress curl on formation of the basin-scale gyres was shown already by Moskalenko (1974). Malanotte-Rizzoli and Bergamasco (1989, 1991) simulated the eastern basin with winds and thermal climatological forcings, whilst Herbaut et al. (1996) studied the western basin in a similar way but with a higher resolution model. Their conclusion was that, in order to produce a circulation with known structures, wind was comparable in importance to heat and water fluxes. Pinardi and Navarra (1993) analyzed the wind-driven component of the Mediterranean Sea general circulation and pointed out the correlation between the sub-basin structures and the curl of the wind stress. Zavatarelli and Mellor (1995), and Roussenov et al. (1995) computed the general circulation solutions with all forcings and for the whole Mediterranean showing the emergence of large-scale gyres and boundary currents due to the combined effect of wind and thermohaline forcing. These studies were done for seasonal climatological equilibrium solutions without much attention to the particular solutions due to wind forcing only. Furthermore, the basin topography can partially control the position of the gyres (Malanotte-Rizzoli and Bergamasco, 1991) but in this paper we want to show that the wind alone can generate upper ocean gyres of observed structure and strength. Thus, our choice is not to have any topography from the start so that a clear demonstration of classical wind stress curl and inertial-viscous boundary layer dynamics can be attained.

Recently, the seasonal and interannual variability of the general circulation has started also to emerge from the data, especially those collected in the eastern Mediterranean (POEM

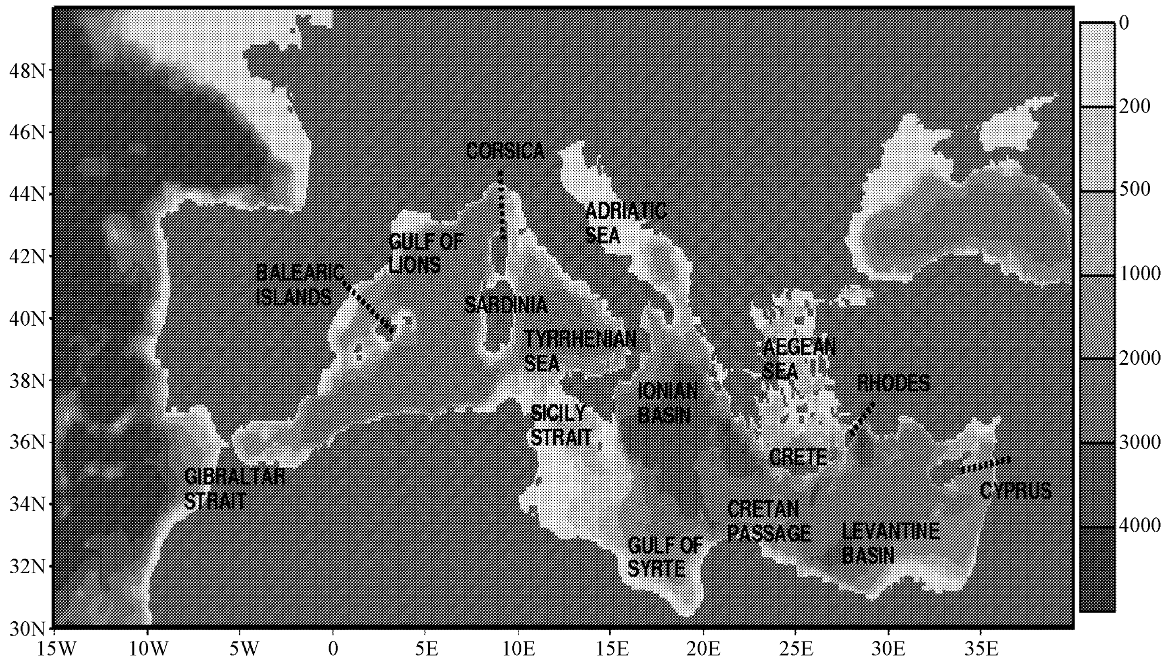

Fig. 1. The Mediterranean basin topography and geographic names.

Group, 1992). Robinson et al. (1991) clarified for the first time that some gyres may be persistent in time while others may be simply non-permanent or recurrent. How can these gyres, equivalent to the sub-polar and sub-tropical gyres of the North Atlantic, be created or missing some years and not others is still an open question which needs numerical and observational studies. The hypothesis is that the variability can be generated by both external forcing and internal non-linear energy redistribution processes, such as hydrodynamical instabilities creating mesoscale eddies which feedback on the mean flow.

Pinardi et al. (1997), Korres et al. (2000a), and Korres et al. (2000b) have shown the possibility of generating interannual variability at the basin scale with atmospheric forcing anomalies. In these studies there are suggestions that wind anomalies may be prominent in generating permanent and semi-permanent gyre variability. In this work, we isolate the wind forcing and examine the solutions in terms of gyres, free and boundary currents and their variability. Our aim is to understand which features of the general circulation variability are produced by wind forcing alone with up-to-date climatological and high-frequency forcing. The other important question is how robust these circulation structures are to details in the wind forcing used, and what part of the wind forcing influences the spatial and temporal variability in the basin.

We use a reduced gravity model which allows us to understand the dynamics of the first baroclinic mode and that encompasses both geostrophic and ageostrophic components. Thus, coastal currents and coastally trapped waves can be studied as a response to winds, a process which has been pointed out to be important also in the past Crepon and Richez (1982). Nevertheless, no study has been done previously to detect coastal signals around the entire Mediterranean basin. However, the Mediterranean Sea has narrow shelves and our solutions does not consider the topographic effects. These results should be then considered preliminary in this respect.

One original aspect of the present work is its computational engine: the Spectral Element Ocean Model (SEOM), originally described in Iskandarani et al. (1995). More recent versions of the model, notably the three-dimensional version, are described in Levin et al. (2000), and Iskandarani et al. (2001). Applications can be found in Curchitser et al. (1999), and Curchitser et al. (2001). SEOM is a relatively new ocean model which relies on the spectral element method to effect the spatial discretization. Its chief features include: a spatial discretization based on unstructured grids, a dual approach to convergence via element or spectral refinement, very low numerical dissipation, and excellent scalability on parallel computers. The most beneficial feature in the context of the present work is the model's ability to describe accurately the highly complex Mediterranean coastline (Fig. 1) without an undue increase in computational cost. In contrast, methods that rely on structured grids, like finite difference methods, must resort to a combination of complicated mappings, very high-resolution grids, and masking to represent the basin's geometry. Numerical methods based on unstructured grids offer an elegant alternative to the structured approach. Furthermore, they allow for local refinement of the grid so that localized small scale dynamical features can be represented efficiently.

In Section 2 we describe the equations solved by the model and the numerical method. Section 3 describes the wind stress data sets; the seasonal and the interannual variability will be analyzed in Section 4. Section 5 presents the analysis of the wind stress curl and Section 6 the process studies. Conclusions are offered in Section 7.

2. Model design

2.1. Equations

The current version of the model (Iskandarani et al., 1995) solves the shallow water equations, written as:

$$\boldsymbol{u}_t + \boldsymbol{u}\cdot\nabla\boldsymbol{u} + f\boldsymbol{k}\times\boldsymbol{u} = -g\nabla\zeta + \frac{\nu}{h+\zeta}\nabla\cdot[(h+\zeta)\nabla\boldsymbol{u}] + \frac{\tau^{\zeta}-\tau^{-h}}{\rho(h+\zeta)} \tag{1}$$

$$\zeta_t + \nabla\cdot[(h+\zeta)\boldsymbol{u}] = 0 \tag{2}$$

where $\boldsymbol{u} = (u, v)$ is the horizontal velocity vector, $\boldsymbol{k}$ a unit vector in the vertical direction, h the resting depth of the fluid, ζ the free surface elevation, f the Coriolis parameter (in the β-plane approximation $f = f_0 + \beta y$, with $f_0 = 2\Omega\sin\theta_0$ and β being the beta parameter evaluated at θ_0), g the gravitational acceleration, ν the viscosity coefficient equal to 300 m^2/s, ρ the homogeneous density of the fluid, $\tau^{\zeta} = (\tau_x^{\zeta}, \tau_y^{\zeta})$ the wind stress acting on the surface of the fluid, ∇ the two-dimensional gradient operator, and τ^{-h} is the stress at the bottom of the fluid. The subscript t denotes differentiation with respect to time. The unknowns are ζ and (u, v).

We suppose that Eqs. (1) and (2) describe the motion of an upper layer of constant density above an infinitely deep and motionless layer. This means that the constant of gravitational acceleration is scaled by the density gradient ($g' = g(\Delta\rho/\rho)$), and ζ is the interface displacement. The model is thus reduced gravity and our value for g' is 6.75×10^{-3} m/s^2. The value of h was chosen to be 300 m corresponding to the depth of the lower boundary of the main thermocline in the Mediterranean Sea denoted by the zero crossing of the first baroclinic mode. This zero crossing is a good approximation for all regions except the shallow Strait of Sicily, Adriatic and Aegean Sea. The surface elevation can be deduced from the interface displacement by the relationship $\zeta_{\text{interface}} = -\zeta_{\text{surface}}(\Delta\rho/\rho)$. Topography and baroclinic instability are not considered.

The stress term τ^{-h} is an interfacial drag term whose role is to prevent the upper layer thickness from vanishing, in which case the lower layer outcrops and reaches the surface. This outcropping problem occurs in the Gulf of Lions where the observed wind-induced cyclonic circulation leads to isopycnal outcropping, and contributes to the preconditioning of deep water formation processes. The interfacial stress is kept small throughout the basin and it is only increased in the Gulf of Lions where it acts to decrease the interfacial slope. The following quadratic law was used to calculate the interfacial stress:

$$\tau^{-h} = -\gamma\boldsymbol{u}^2 \tag{3}$$

$$\gamma = \gamma_{\min} + \tfrac{1}{2}(\gamma_{\max}-\gamma_{\min})(1+\tan(r_0^2-r^2)) \tag{4}$$

where r is the radial distance from the center of the Gulf of Lions gyre, r_0 the influence radius and $(\gamma_{\min}, \gamma_{\max})$ is the minimum (outside the circle of radius r_0) and the maximum (within r_0) friction. In our simulations, r_0 is 50 km and γ ranges from 0.0025 in the far field to a maximum of 0.01 in the Gulf of Lions. All simulations use the same interfacial stress formulation.

2.2. Numerical aspects

The spectral element method is an h–p-type finite element method which combines the geometrical flexibility of traditional (low order) finite element methods with the rapid convergence rate of spectral methods. The spatial discretization relies on an unstructured partitioning of the basin into quadrilateral elements within which the solution is interpolated with a relatively high-order polynomial. The error can be decreased either by increasing the number of elements (h-refinement), in which case the error decreases at a fixed high-algebraic rate, or by increasing the polynomial order (p-refinement) which results in an exponential convergence rates for smooth solutions. The optimal combination of order and number of elements is problem dependent: complex basin geometries and rapidly varying solutions favor h-refinement, while regular geometries and smooth solutions are computed more efficiently via p-refinement.

Unstructured grids offer several desirable properties for oceanic simulations. First, unstructured grids are highly flexible and permit a faithful representation of the coastline with fewer degrees of freedom than other discretization methods. Second, multi-scale simulation capabilities are possible and easy to implement: the resolution can be increased locally to capture small dynamical feature without an undue increase in computational cost over the entire domain.

The spectral nature of SEOM offers the possibility of computing accurate solutions efficiently. The most valuable features in the numerical oceanic circulation context are low numerical dispersion errors, which result in accurate representation of phase speeds, and very low numerical diffusion errors. Furthermore, the local and dense nature of the computations make the method ideally suited for parallel computers (Curchitser et al., 1998). The code used in the simulations herein was optimized for the CRAY-T3E by overlapping communication and computations, and by relying on one-sided message passing to reduce message latency. These improvements resulted in a linear scaling of the efficiency regardless of the mapping between the sub-domains and the physical processors (Molcard et al., 1998). The simulations presented herein were run on 128 CRAY-T3E processors. A 1-year simulation required 5 min of CPU.

For further details on the numerical formulation we refer the reader to Iskandarani et al. (1995), Levin et al. (2000), and Iskandarani et al. (2001). Applications of the various versions of the model can be found in Curchitser et al. (1999, 2001), and Perenne et al. (2001). Finally, we mention that an atmospheric version of the model has been developed. Taylor et al. (1997), and Wingate and Boyd (1996) have produced a triangular spectral element shallow water model. In the remainder of this section we focus exclusively on the numerical implementation for the Mediterranean Sea.

Fig. 2 shows the elemental decomposition of the domain. The grid consists of 681 elements with a seventh-order polynomial for the velocity, leading to 25,430 nodes, and a fifth-order polynomial for the pressure field, leading to 11,504 nodes. This difference in order is required to suppress spurious pressure modes (Iskandarani et al., 1995). The grid resolution varies from 1 to 25 km, with an average resolution of 10 km. This variable mesh refinement is necessary to focus our interest in regions where complex dynamical phenomena occurs (as Gibraltar and Sicily straits, the Gulf of Lions), and to properly follow the complex coastline.

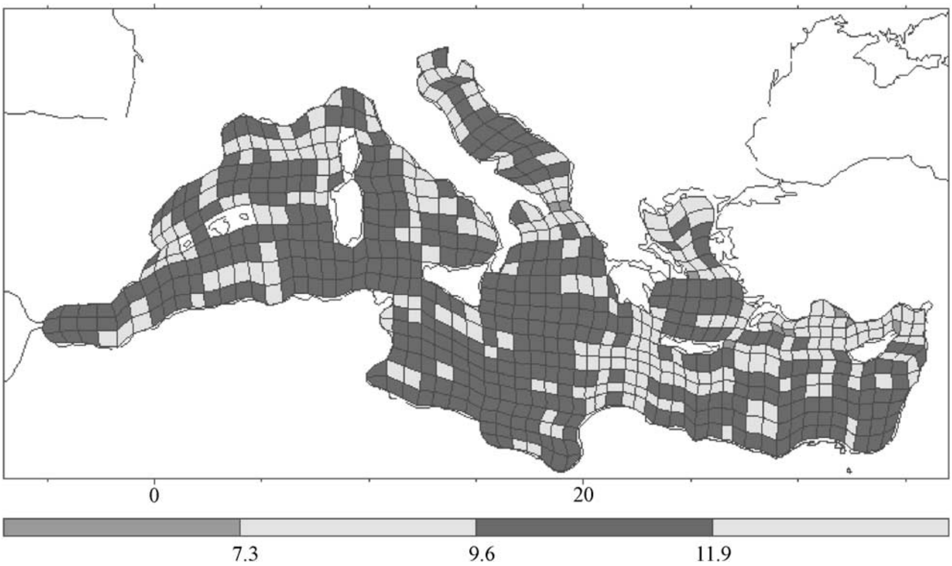

Fig. 2. Distribution of spectral elements: the greyscale bar represents the average grid spacing in km for each element.

The time integration relies on an explicit third-order Adams Bashforth scheme and the time step used is 240 s. This limit is dictated by the fastest propagating waves which in our case are the gravity waves. In the reduced gravity case their propagation speed (m/s) is:

$$c = \sqrt{g'h} = \sqrt{g\frac{\Delta\rho}{\rho}h} \approx 2 \tag{5}$$

3. Forcing

The aim of this study is to analyze the wind-driven response of the Mediterranean Sea general circulation, and in particular its seasonal and interannual variability.

However, wind data sets and computations of wind stresses may be affected by many sources of errors. First, observations mostly exist at land stations (near the shores) and wind values at sea may not be easily extrapolated from such sampling. Ship of opportunity wind measurements are also coarse and sporadic while numerical weather forecast models do not have adequate resolution to resolve the orography of the basin (Cavaleri and Bertotti, 1997). Thus, different wind data sets may be affected by different sources of errors even if they may represent part of the real signal. The analysis of wind stress reliability in the Mediterranean Sea is out of the scope of this paper but we acknowledge from the start that large discrepancies may occur between different wind data sets. In addition to the problem of accuracy of wind stress data sets, the Mediterranean Sea circulation is affected by large-amplitude variability at seasonal and interannual time scales (Korres et al., 2000b;

Samuel et al., 1998) which can in turn affect our estimation of the wind stress in the region. Samuel et al. (1998) examined the response of a model forced by two climatological wind stress data sets generated by averaging in two distinct periods, the first 1980–1987, and the second 1988–1993. The latter period is shown to be different from the first and from old climatologies such as those in Hellerman and Rosenstein (1983) computed with 100 years of data. The ocean simulation showed remarkable differences due to the two forcing climatologies. Horton et al (1997) improved the boundary layer model formulations used to deduce surface winds in order to retain a more accurate representation of orographic effects. The ocean simulations produced with the modified winds showed an improvement with respect to observations.

In this paper we use two wind stress data sets in order to evaluate the robust features of the circulation. If differences arise, we will try to interpret them on the basis of the differences in forcing. The two data sets used are the COADS (Da Silva et al., 1995) wind stress and a stress computed from 10 m winds of the European Center for Medium Range Weather Forecast (ECMWF), Reading, UK, atmospheric model operational re-analysis project (ERA, acronym for ECMWF Re-Analysis). The COADS wind stresses are available monthly on a $1^\circ \times 1^\circ$ grid while the ERA winds are available every 6 h on a $1.26^\circ \times 1.26^\circ$ degree grid. Wind stresses are computed using the bulk formula:

$$(\tau_x^\zeta, \tau_y^\zeta) = \rho C_\mathrm{D}|w|(w_x, w_y) \tag{6}$$

where w is the 10 m wind speed and subscripts x and y denote zonal and meridional components. The drag coefficient C_D is computed by the relationship suggested by Smith (1980). From the 6 h winds, monthly mean wind stresses were then computed and used in the integrations.

The COADS and ERA wind stresses are different in intensity and structure, even though they maintain some important features of the stresses known to occur in the Mediterranean (Pinardi and Navarra, 1993; Cavaleri and Bertotti, 1997). Figs. 3 and 4 represent the monthly mean wind stress and curl from COADS and ERA data for January, April, July and November. These months fall within the season definition of Hecht et al. (1988). The intensity is comparable but the horizontal structure and the seasonal variability are very different. The winds from COADS are smooth and the curl presents large structures whilst the ERA winds are much more variable in space and time. In both of them we recognize the dipolar curl structure in the western Mediterranean due to the Mistral winds and the dipolar structure due to Etesian winds over the Aegean and Levantine basins. The largest differences are in the Ionian and Tyrrhenian basins.

Fig. 5 shows the time series of the area averaged monthly mean wind stress magnitude over the Mediterranean Sea for the two data sets. The good correlation between the two data sets is evident but there are consistent differences in intensity especially during the summer months. Etesian winds seem to be consistently larger in COADS than ERA (see July–September peaks in COADS) while the location of the winter peaks is synchronous in the two data sets. Both data sets show large-amplitude interannual variations in the winter months, with the largest positive anomalies in the January of 1988 and 1992.

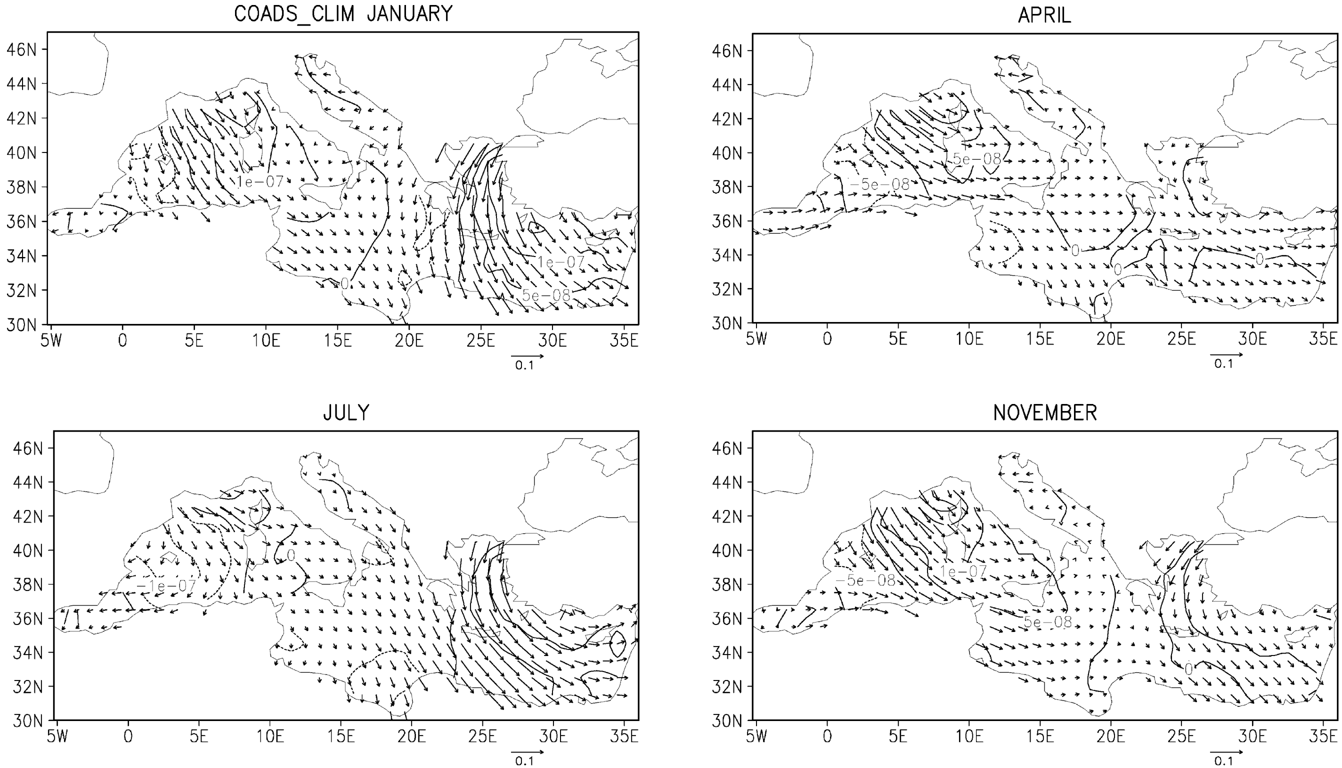

Fig. 3. COADS wind stress (N/m^2) vectors superimposed on curl amplitude contours (N/m^3). The reference arrow is shown below each picture.

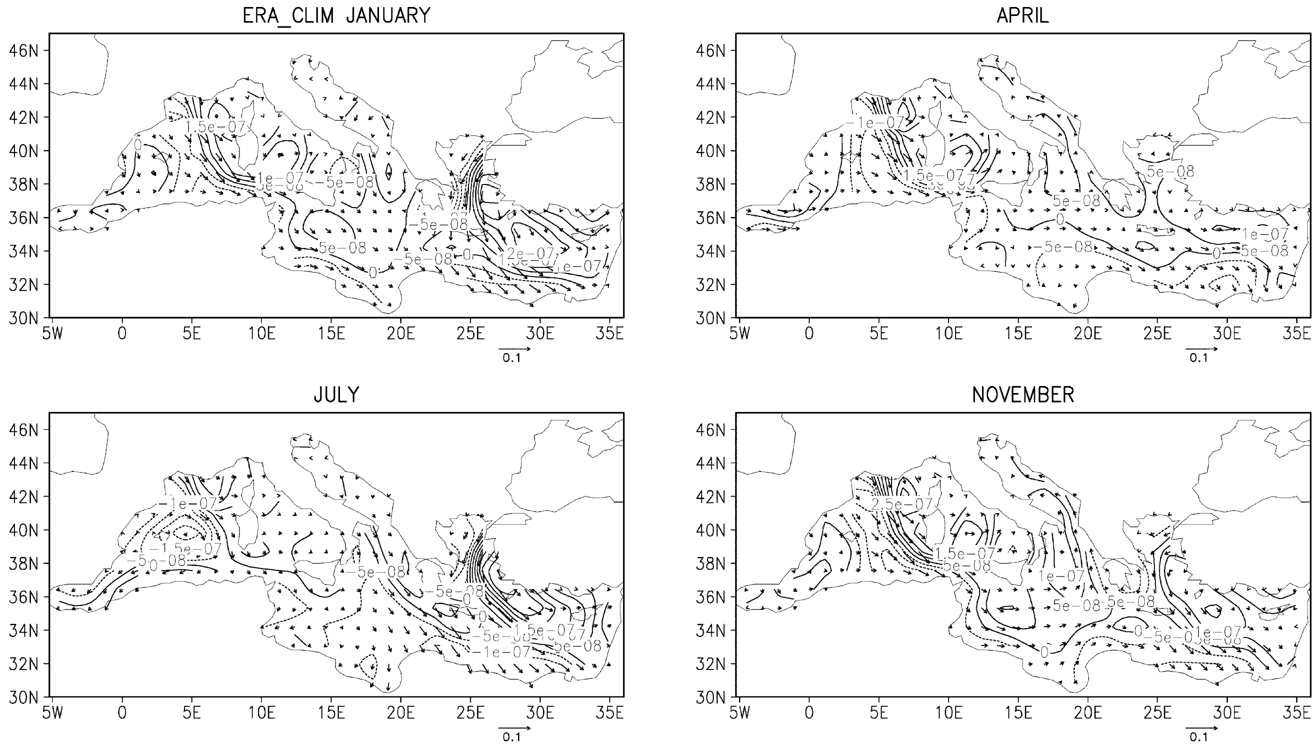

Fig. 4. ERA wind stress (N/m^2) vectors superimposed to curl amplitude contours (N/m^3). The reference arrow is shown below each picture.

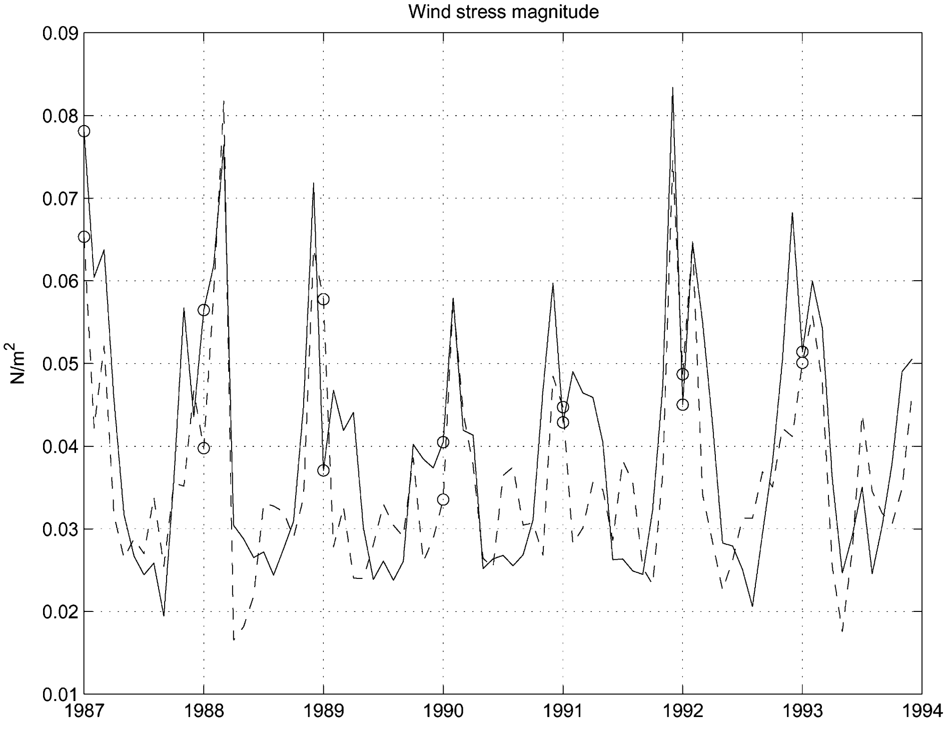

Fig. 5. Basin averaged wind stress magnitude: ERA full line, COADS dashed line. The symbol '○' indicates the months of January for each data set.

4. Seasonal and interannual variability

Table 1 lists the runs that have been carried out in order to analyze the seasonal and interannual variability of the wind-driven circulation. The wind stress climatology from Hellerman and Rosenstein (1983) is used to stabilize the model and to calibrate the viscosity

Table 1
List of numerical experiments

Simulation	Forcing	Period	Process
HR	Hellermann and Rosenstein	5 Years	Spin-up
ERA	ECMWF reanalysis 10 m	January 1987–December 1993	Seasonal and interannual variability
COADS	COADS 10 m	January 1987–December 1993	Seasonal and interannual variability
ERAEOF1	EOF1 of ERA	January 1987–December 1993	Wind-driven dynamics
ERAX2	ERAX2	January 1987–December 1993	Intensity of winds
ERAFILT	ERA filtered	January 1987–December 1993	Spatial structure of winds
COADSNOBETA	COADS	January 1987–December 1993	$\beta = 0$

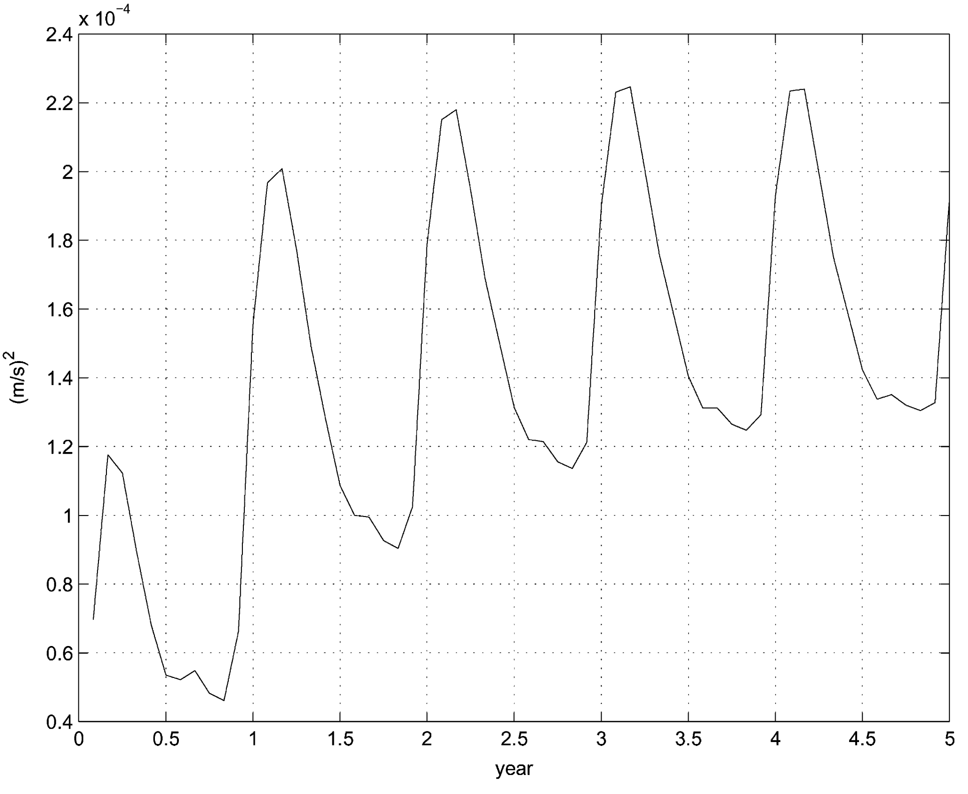

Fig. 6. Basin averaged kinetic energy in (m/s^2) for the HR simulation.

parameters. After achieving a repeating seasonal cycle (Fig. 6) interannual simulations are carried out with the two wind stress data sets for the period January 1987–December 1993.

Fig. 7 represents the kinetic energy of the circulation for the two interannual simulations. The lines are in phase but the response to the ERA forcing is larger in amplitude than to COADS. The correspondence between the response and the wind stress can be easily seen by comparing Figs. 5 and 7. Strong wind events (like in 1988, 1992) accelerate the mean circulation while the weakened winds in the period 1989–1991 causes a large decrease in the kinetic energy of the response. In addition not all the wind stress anomalies generate a peak in the kinetic energy. In fact the 1989 wind stress anomaly does not correlate with a circulation kinetic energy peak, while the 1992 wind stress anomaly does. This was found already by Korres et al. (2000a) and it may be related to processes of ocean memory and the dependence of the solution from the oceanic circulation state present before the winter wind event. The non-linear response to the winds in the 1989–1991 period is now also analyzed by Demirov and Pinardi (2001) in a three-dimensional model of the general circulation.

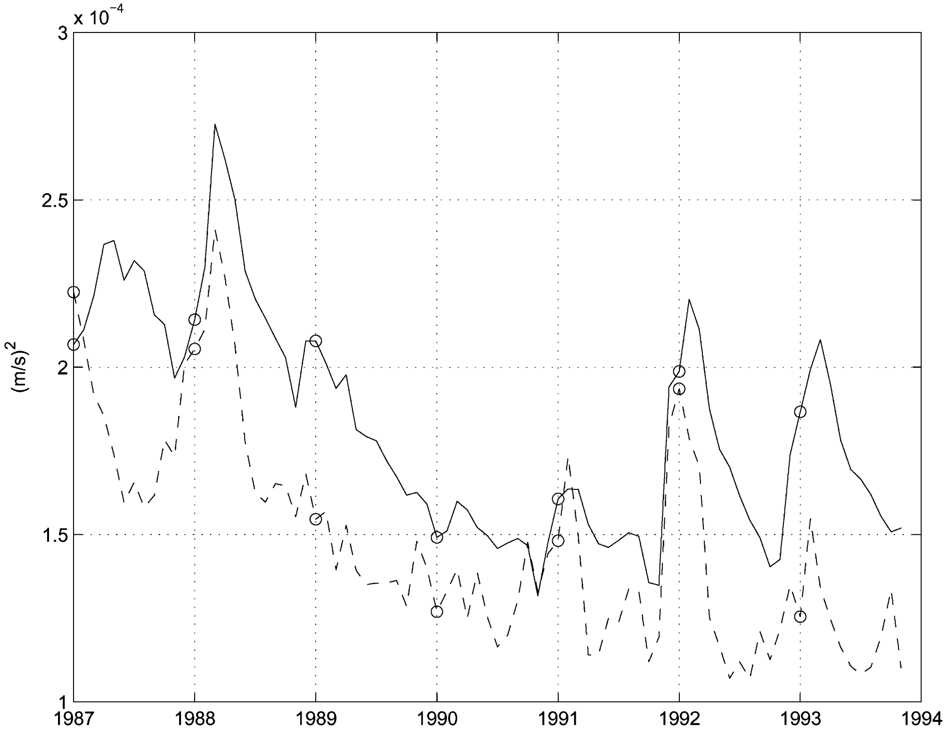

Fig. 7. Basin averaged kinetic energy in $(m/s)^2$ for the two simulations ERA (full line) and COADS (dashed line). The symbol '○' indicates January months for both simulations.

4.1. Seasonal analysis

The seasonal variability of the circulation is shown in Figs. 8 and 9 for COADS and ERA forcings, respectively. The average is done for January and July months of the 7-years simulation. The circulation is composed of sub-basin scale gyres due to the major wind stress curl centers shown in Fig. 3 and 4. The important thing to notice is that even if wind stress curl is different between ERA and COADS the structure of the seasonal circulation is approximately the same. The first result is that some features compose the seasonal cycle independently from the forcing used. These structures are the Gulf of Lions gyre, the Rhodes gyre and the anticyclonic gyre in the Gulf of Syrte. The Gulf of Lions and the Rhodes gyres also show boundary intensified northern currents which are part of the dynamical response to winds, as explained later in Section 5. These permanent structures are always recognizable in the same location and have small seasonal changes in amplitude. We then conclude that the steady-state component of the wind-driven circulation is large probably due to a non-linear rectification of the time-dependent vorticity input.

The seasonal variability of the circulation involves the changes in strength of the southern current in the Algerian basin, the northward current in the Tyrrhenian basin, the Adriatic and Aegean circulations and the eastern Levantine basin boundary currents. In this region,

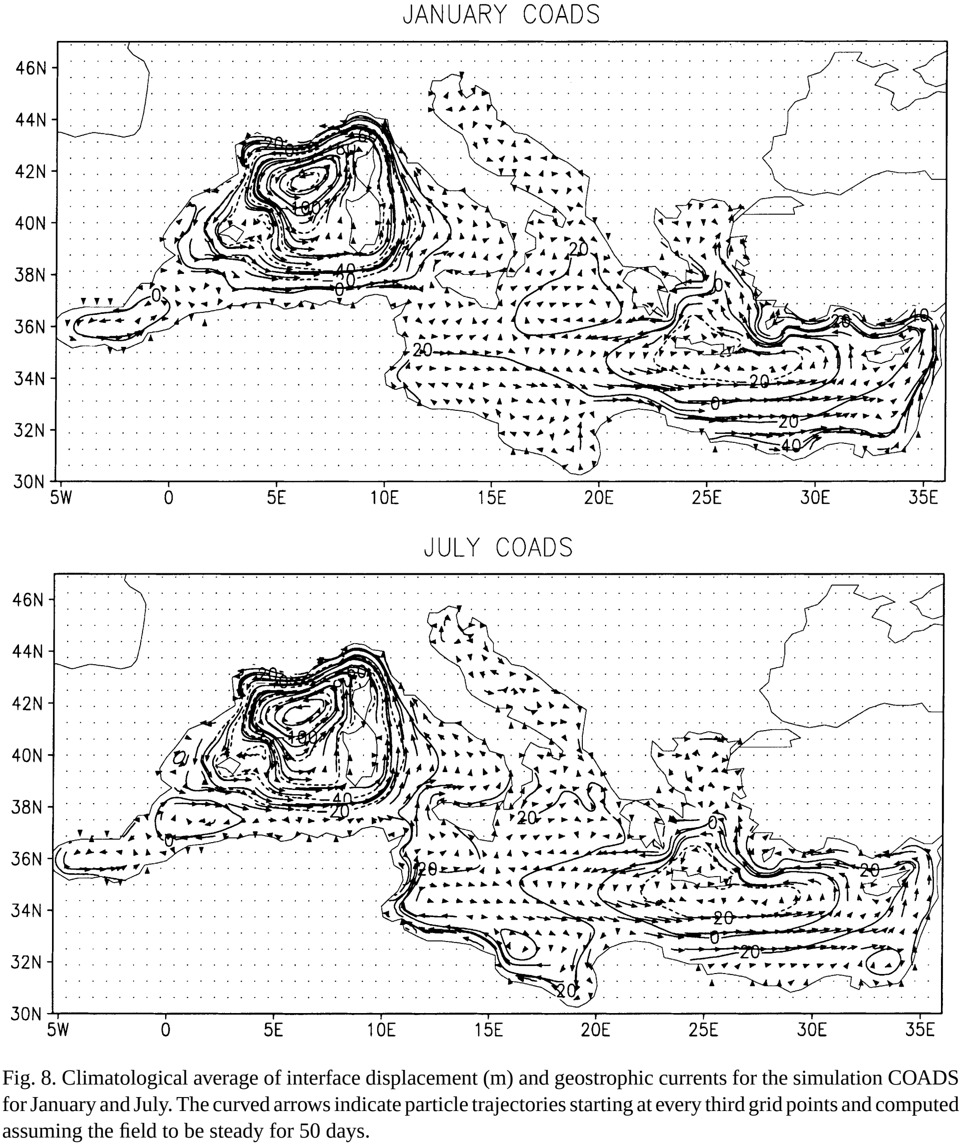

Fig. 8. Climatological average of interface displacement (m) and geostrophic currents for the simulation COADS for January and July. The curved arrows indicate particle trajectories starting at every third grid points and computed assuming the field to be steady for 50 days.

the anticyclonic area present in the southeastern Levantine during July vanishes in January, where a boundary current appears to hug the coast. This is present in both COADS and ERA simulations and we consider this a robust feature of the seasonal cycle in the basin. Another seasonal change, occurring in both simulations, involves the strength of the northern Levantine boundary current corresponding to the Asia Minor Current, first described by Robinson et al. (1991).

The seasonal and interrannual variability of this period (1987–1993) is analyzed using the Empirical Orthogonal Function (EOF) method ((Emery and Thomson, 1997; Korres

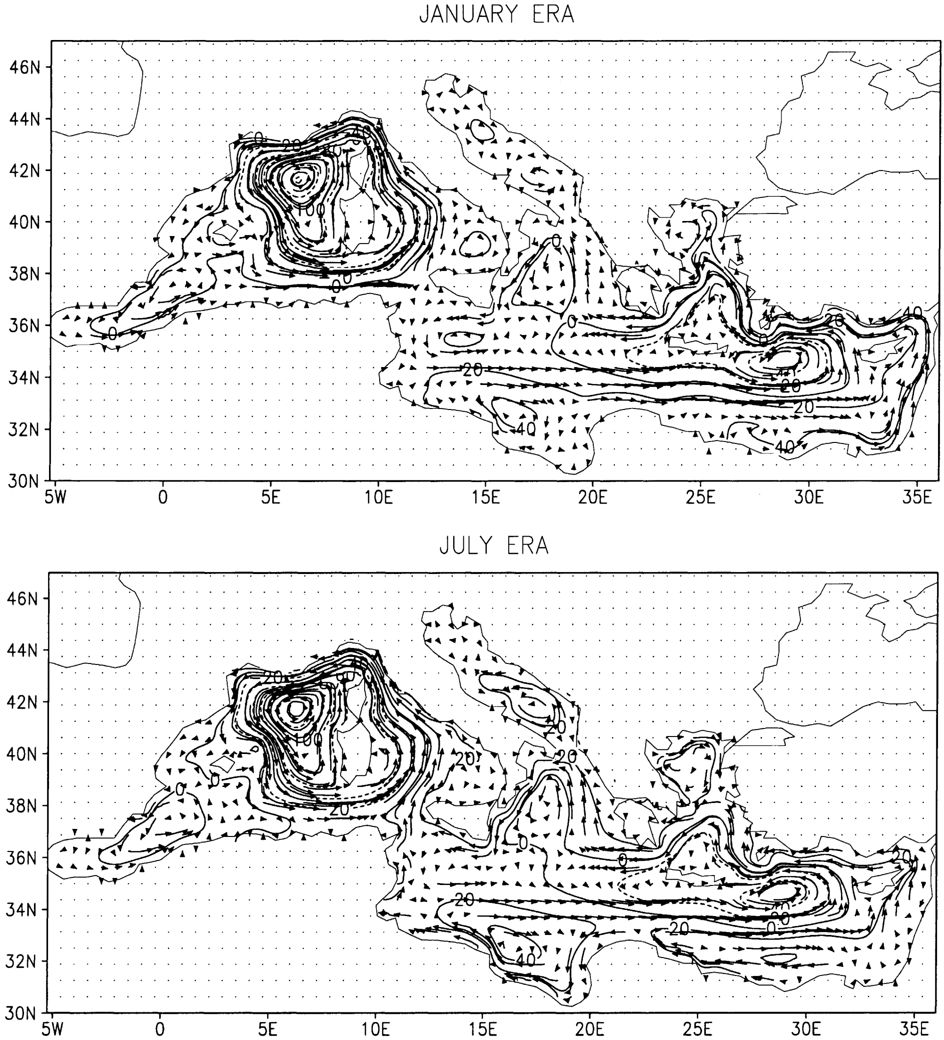

Fig. 9. Climatological average of interface displacement (m) and currents for the simulation ERA for January and July. The curved arrows indicate particle trajectories starting every three grid points in the mesh and computed assuming the field to be steady for 50 days.

et al., 2000b)). This statistical tool is useful to extract the temporal and spatial variability from a large data set. Two different anomalies are analyzed, one obtained by subtracting from the initial data the steady-state mean (referred to as SS anomaly) that will contain both seasonal and interannual variability, and the second generated by subtracting the seasonal cycle (referred to as SC anomaly) that will contain only the interannual variability.

The EOF method decomposes the signal in spatial modes and amplitude time series that describe the time evolution of the data. Thus, the interface displacement anomaly ζ is

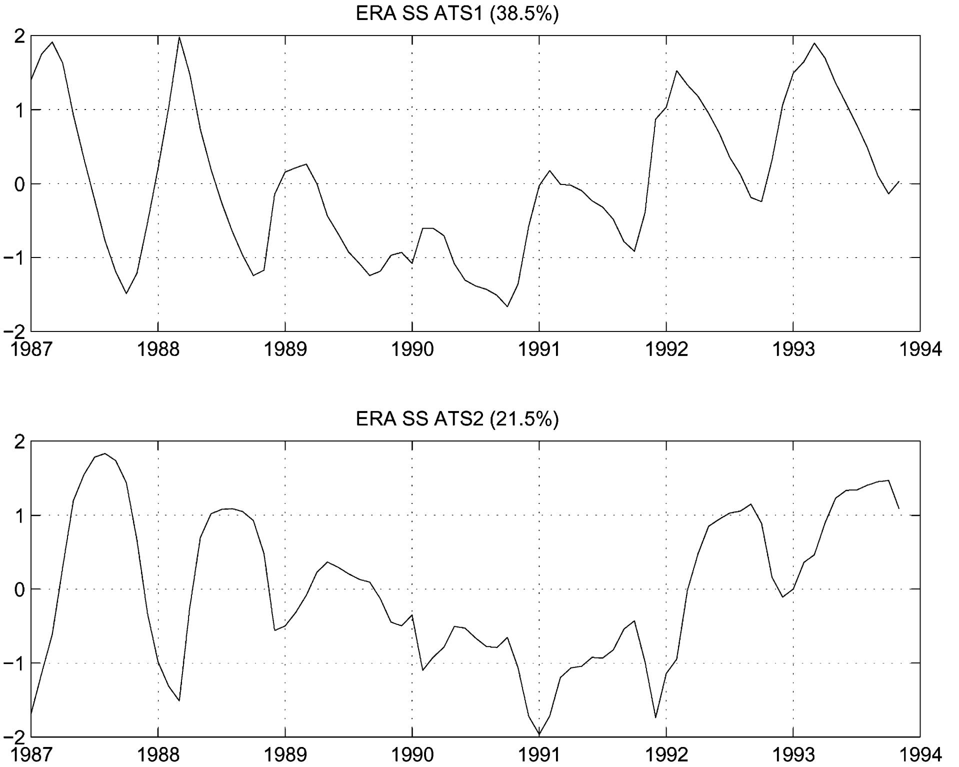

Fig. 10. Amplitude time series associated with the first (ATS1 upper panel) and the second EOF (ATS2 lower panel) for the ERA experiment. The anomalies are calculated substracting the steady-state mean (SS). Numbers in parenthesis at the top of the figures indicate the variance accounted for by each EOF.

represented by:

$$\zeta(x, y, t) = \sum_{k} a_k(t) e_k(x, y) \tag{7}$$

where $a_k(t)$ is the amplitude time series of the k_{th} mode and $e_k(x, y)$ its horizontal structure. A trend is subtracted from the simulations before applying Eq. (7).

The EOF components of the SS anomalies from the ERA simulation are displayed in Fig. 10 for the amplitude time series. These first two EOF account for about 60% of the total variability. In Fig. 10, the two amplitude time series associated with first and second EOF show a clear seasonal signal, more intense in the first two and last 2 years of the time series. Furthermore, the differences between successive minima and maxima in the seasonal cycle show that the interannual variability is coupled to the seasonal cycle in amplitude and phase. This means that the seasonal cycle will have different amplitude in different years (as for example is shown by the different amplitude of the seasonal cycle in 1988 and 1990). Furthermore, the timing of amplitude maxima will be different between years, such as for the winters of 1988 and 1989. We call this a phase shift of the seasonal cycle due to the interannual variability.

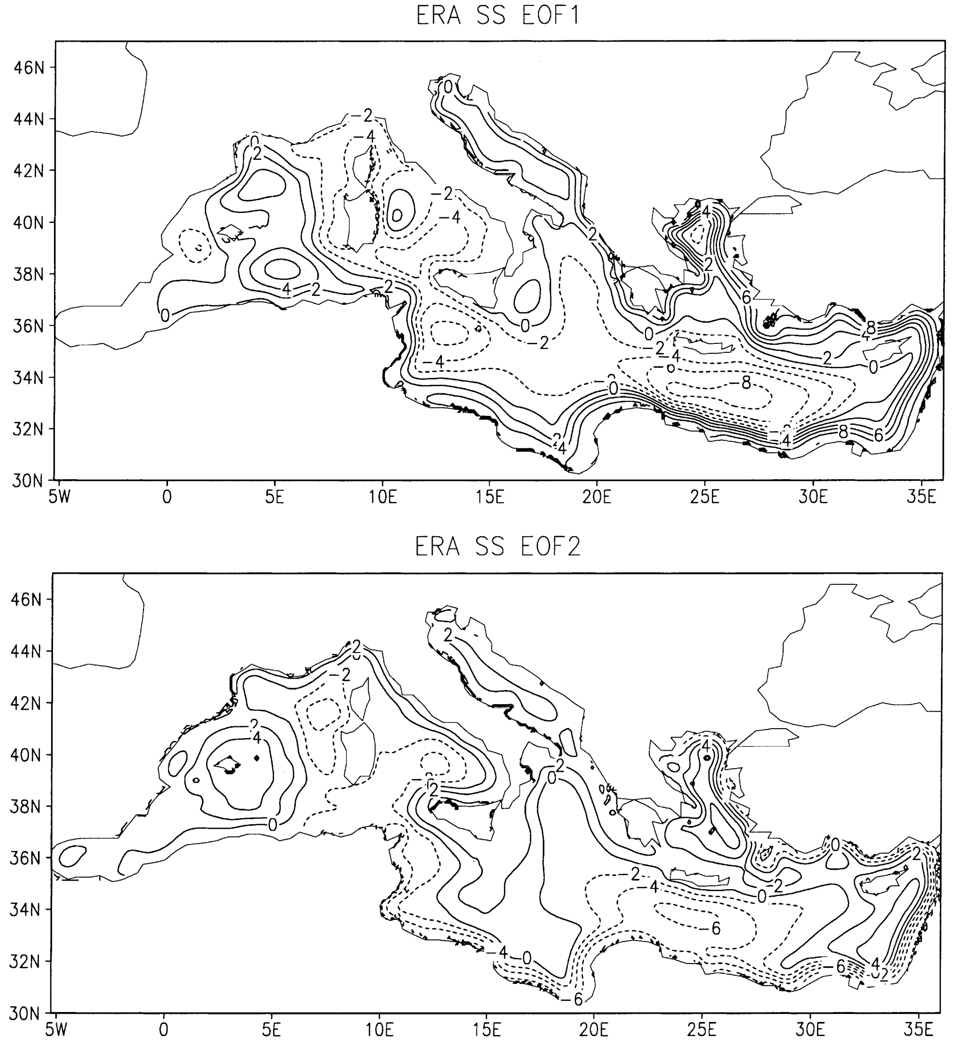

Fig. 11. Spatial structure of the first (upper panel) and second EOF (lower panel) for the experiment ERA and the SS anomalies.

The spatial structures associated with the first two EOF are shown in Fig. 11. The first mode that contains 38.5% of the total variance is characterized by large structures in the Levantine basin–Cretan passage and in the Gulf of Lions–Algerian basin. Dipolar smaller scale gyres appear in the Tyrrhenian and Ionian Sea. The first EOF amplitude maxima is reached along the Levantine basin coastlines clearly showing that the seasonal weakening and strengthening of these boundary current regions is a major component of the seasonal cycle in the basin. The second mode shows smaller spatial structures than the first with the exception of the Ionian and Tyrrhenian basins. Also the sign of the two EOF are different in the Sicily Strait and in the Levantine basin. The dipolar structures in the Gulf of Lions can be visually connected to the wind stress curl dipoles present in Fig. 4. This strengthens the evidence that a time-dependent Sverdrup balance with boundary layers is forced by the wind stress curl. Time-dependent wind-driven currents have been recently studied by Pierini (1998). Our solutions are similar to the fluctuating solutions of Pierini (1998) in the inertial-viscous regime, e.g. the dynamical balance where the wind stress curl, the linear (β and the viscosity) and non-linear terms are all important. This discussion will be continued in Section 5.

4.2. Interannual variability

The same EOF analysis is done with the SC anomalies for the ERA simulation in order to isolate the interannual signal. The seasonal interface displacement removed is the one presented in Fig. 9.

Fig. 12 represents the amplitude time series (ATS) associated with the first and second EOF and clearly shows the interannual variability contained in this simulation. The total variance explained by the first two modes is approximately 60%. The largest amplitude interannual variability is achieved from 1989 to 1991, in the central period of the time

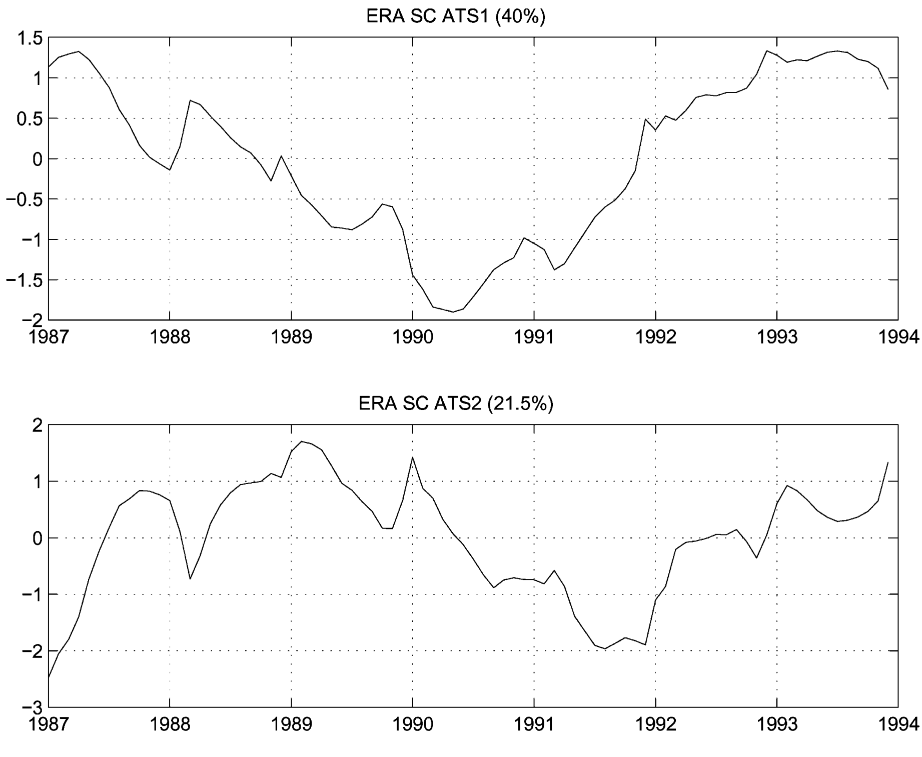

Fig. 12. Amplitude time series associated with the first (ATS1 upper panel) and the second EOF (ATS2 lower panel) for the ERA experiment. The anomalies are calculated substracting the monthly mean seasonal cycle (SC). Numbers in parenthesis at the top of the figures indicate the variance accounted by each EOF.

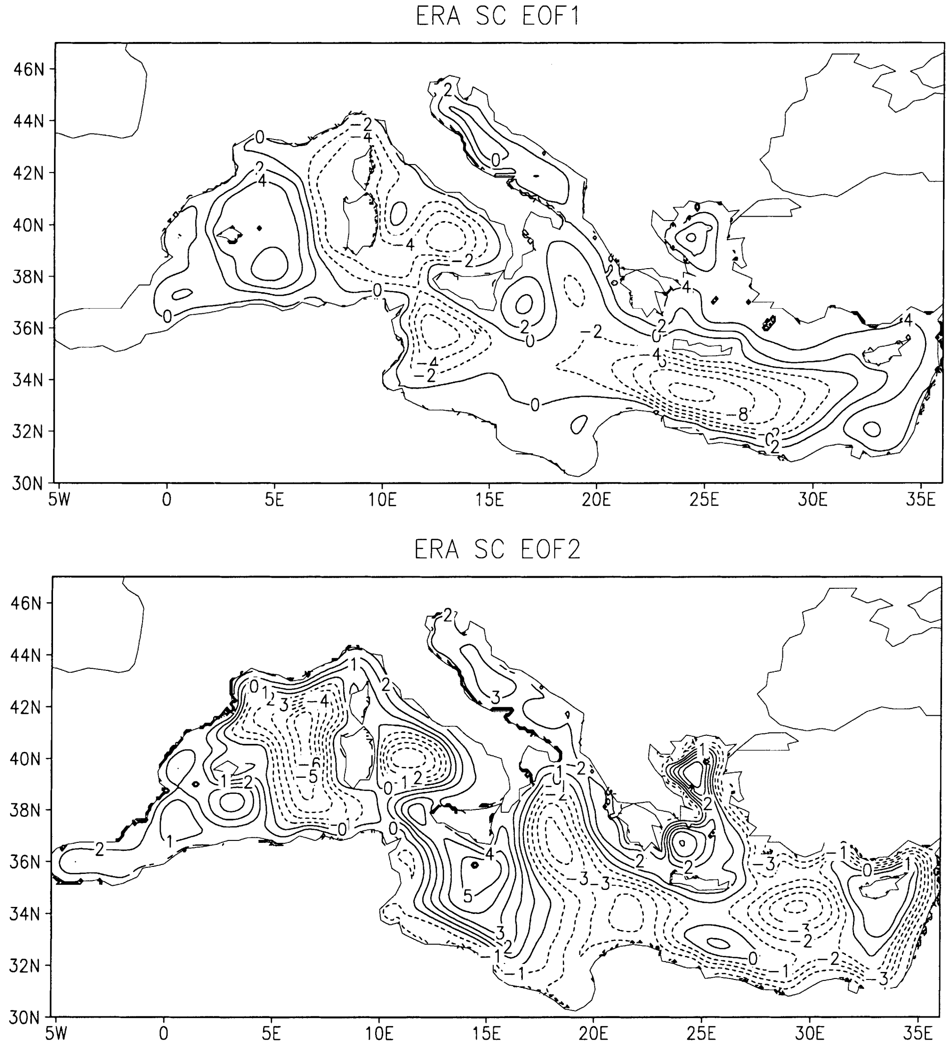

Fig. 13. Spatial structure of the first (upper panel) and second EOF (lower panel) for the experiment ERA and the SC anomalies.

series, where the circulation had minimum kinetic energy (see Fig. 7), just the opposite of the seasonal cycle amplitude which is largest in the 1987–1988 and 1992–1993 periods (see Section 4.1).

The spatial structures associated with the first two EOF of the SC anomalies are represented in Fig. 13. The first EOF is similar to the SS anomalies EOF described earlier confirming that seasonal and interannual variability modes have substantially the same horizontal structure. The largest difference between the first SS EOF and the first SC EOF is in the Levantine basin where the SC EOF does not show any boundary current intensification.

This means that the Levantine basin boundary current intensification/weakening phenomena is mostly linked to the averaged seasonal cycle. However, interannual variability of such boundary currents is present in the second SC anomaly EOF which accounts for 21% of the variability. Thus, the Levantine basin boundary current changes are characterized by both averaged seasonal (SS EOF1 and EOF2) and interannual time scales (SC EOF2).

It is interesting now to reconstruct the interannual changes from the first SC EOF patterns (Fig. 13) and the respective amplitude time series (Fig. 12). The periods 1987–1988 and 1992–1993 corresponds to an amplification of the eastern basin cyclonic gyres, as seen by the fact that the amplitude time series is positive and the structures by the first EOF are cyclonic. In the western basin, the cyclonic gyre circulation is weakened in the Catalan Sea (between the Spanish coasts and the Balearic islands) and strengthened in the Tyrrhenian Sea. During the period 1989–1991, the interannual changes are just the opposite since the amplitude time series show negative values. Thus, during the period 1989–1991, the western basin Gulf of Lions cyclonic gyre is strengthened and the Levantine basin circulation weakened. For the Gulf of Lions circulation, the reconstructed field by the second SC EOF has larger amplitudes and should be also considered. In this region, the two EOF spatial structures and the two amplitude time series show a shift in space and in time of the cyclonic circulation.

5. Time-dependent wind-driven dynamics

The large-scale ocean circulation at mid-latitudes is controlled by the curl of the wind stress. The large-scale ocean dynamics at long time scales (with respect to geostrophic adjustment) is regulated by the quasi-geostrophic vorticity equation deduced from Eqs. (1) and (2):

$$\frac{\partial \xi}{\partial t} + \vec{v} \cdot \vec{\nabla} \xi + \beta v = \hat{k} \cdot \nabla \times \left[\frac{\tau^{\zeta}}{h+\zeta} \right] - \hat{k} \cdot \nabla \times \left[\frac{\tau^{-h}}{h+\zeta} \right] \tag{8}$$

where we have neglected the horizontal viscosity terms since ν is small. Here $u = -(g'/f)(\partial \zeta / \partial y)$, $v = (g'/f)(\partial \zeta / \partial x)$ and $\xi = (\partial v / \partial x) - (\partial u / \partial y)$ is the vorticity and the interface displacement, ζ is proportional to the streamfunction of the flow field. If the curl of the wind stress has positive (negative) values within the basin then the circulation may be composed of cyclonic (anticyclonic) gyres with inertial-viscous boundary layers along the lateral boundaries. These inertial layer thickness is given by $\delta_{\mathrm{I}} = \sqrt{u/\beta}$ where $u = \tau_0/\rho h \beta L$ (Pedlosky, 1987). For the Mediterranean $L = 200\,\mathrm{km}$, $h = 300\,\mathrm{m}$ and $\tau_0 = 0.2\,\mathrm{dyn/cm^2}$ which gives $\delta_{\mathrm{I}} \sim 40\,\mathrm{km}$. The viscous boundary layer thickness due to τ^{-h} is smaller than δ_{I}, between 4 and 10 km. Thus, we define our boundary layers to be in the inertial-viscous regime without differentiating between the two components.

As shown in the previous section, our boundary currents are approximately 30–50 km in width, demonstrating that inertial-viscous boundary layers exist at the rim of gyres. These boundary layer currents have a large steady-state component (as for the case of the Gulf of Lions northern current) but they also fluctuate seasonally as for the case of the Levantine basin (current along the eastern and northern basin coastlines). We want to show now that a time-dependent correlation exists between the wind stress curl structure and the gyres

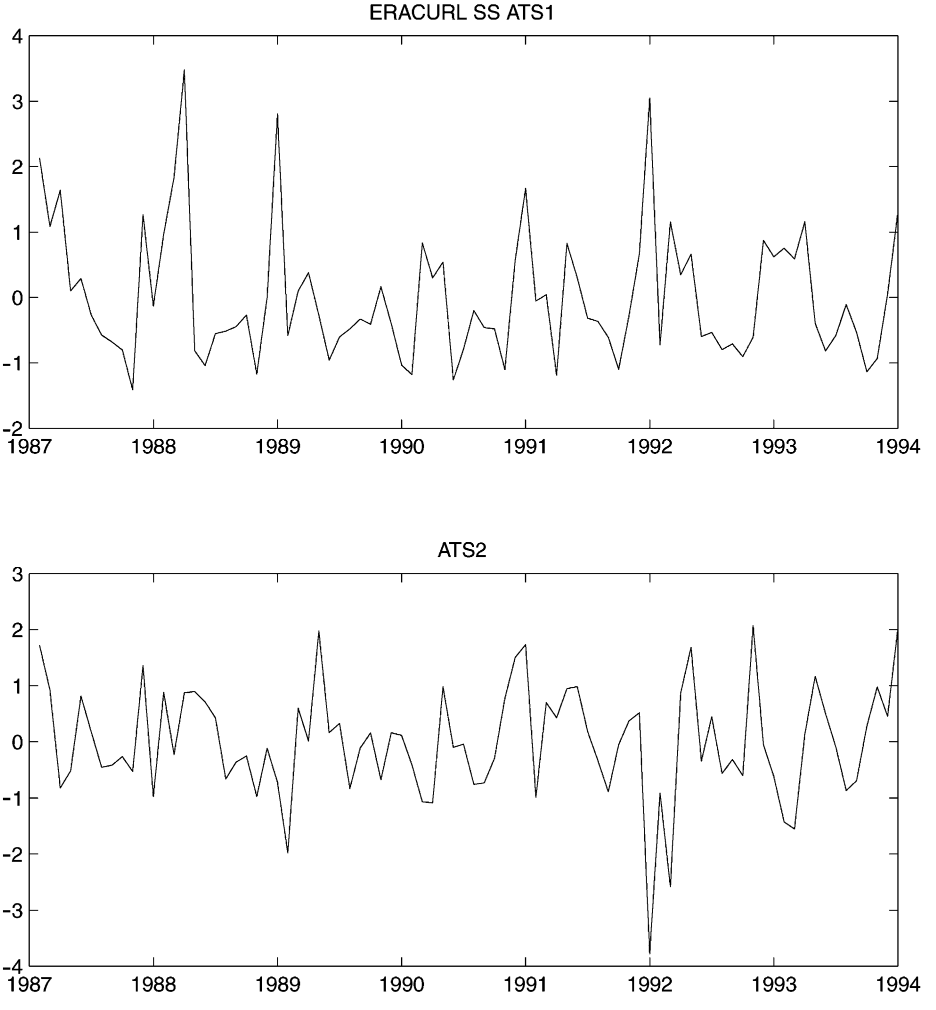

Fig. 14. Amplitude time series of the first (ATS1 upper panel, 30% of the total variance) and second EOF (ATS2 lower panel, 20% of variance) for ERA wind stress curl SS anomalies.

appearing in the ocean response. This way we extend the traditional steady-state Sverdup balance dynamics to the time-dependent case.

In order to show this correlation, the EOF analysis is applied to the wind stress curl from the ERA data set. Fig. 14 represents the amplitude time series for the SS curt anomalies. The first two modes contain 50% of the total variance. The seasonal and interannual variability of the wind stress curl is clearly shown in the amplitude time series. The second amplitude time series shows an intense interannual signal, and a strong anomaly event in winter 1992.

The curl EOF spatial structures are depicted in Fig. 15. Comparing the latter with Fig. 11, it is possible to see that: (1) the double-gyre structure in the Gulf of Lions is associated with the opposite sign wind stress curl centers; (2) the large-scale positive curl vorticity input

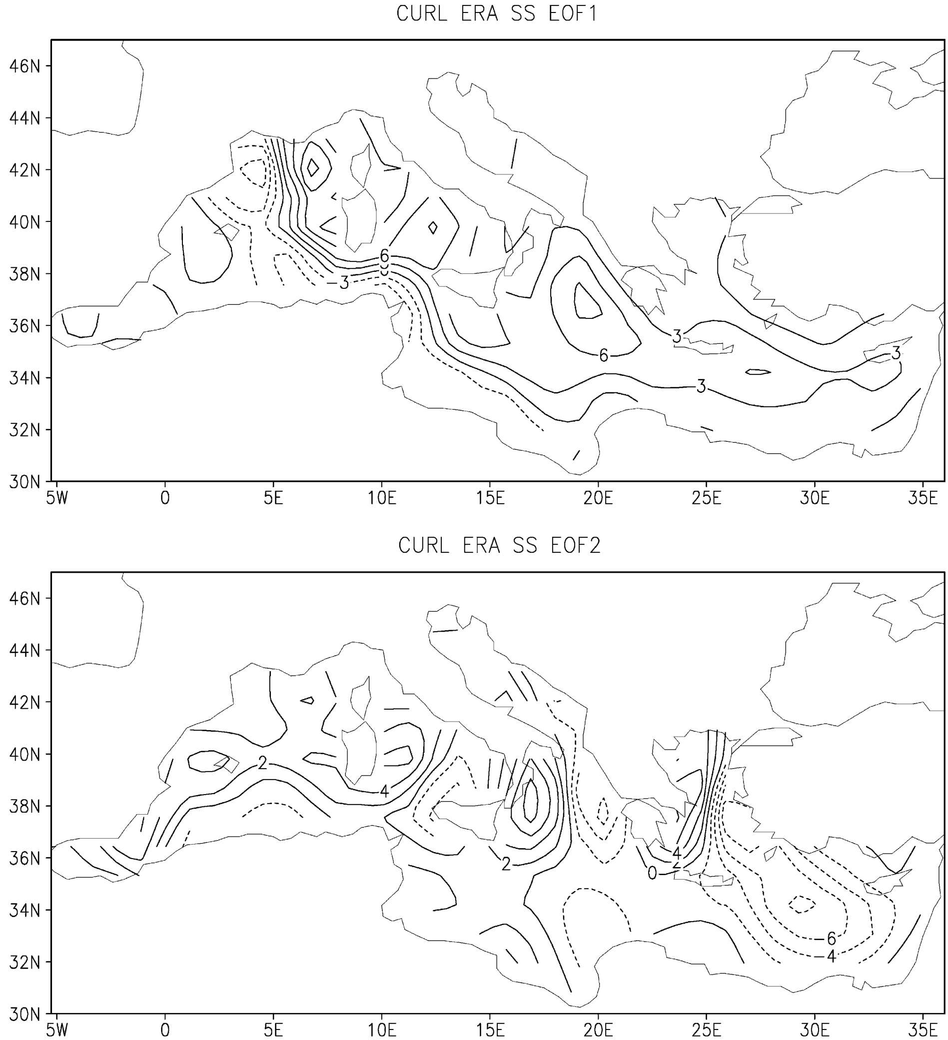

Fig. 15. Spatial structure of the first (upper panel) and second EOF (lower panel) for the ERA wind stress curl SS anomalies.

in the Ionian and Levantine basins can be connected to the large-scale cyclonic circulation in the SS anomaly first EOF, and (3) the second EOF curl double dipole structure in the Tyrrhenian and Ionian Sea can be related to the first EOF dipolar structures in the same areas.

From Figs. 11 and 15 it is evident that the horizontal structure of the time-dependent ocean response is connected to the wind stress curl structure in a way similar to the steady-state balance in classical Sverdrup gyres. In order to quantify this analogy we proceed in two different ways. Firstly, we compute the correlation coefficient between wind stress curl and ocean response. As a matter of comparison, the classical Stommel solution is correlated with the wind stress curl in Appendix A. We can show then that, in the classical steady-state Stommel sub-tropical gyre solution, the maximum correlation is -0.61. The degree of correlation decreases as the boundary layer thickness increases, as expected. In our case, we compute the correlation coefficient between the first curl EOF structure (Fig. 15) and the first EOF of the ocean response (Fig. 11). The correlation coefficient range between -0.56 and -0.64 depending on the sub-basin chosen. This demonstrate that a time-dependent Sverdrup gyre balance exists at the level of the first EOF. For the second EOF, the correlations are much lower indicating a dominant non-linear dynamics in the interior of the basin.

The second method used to show that a time-dependent vorticity balance exists for each EOF mode is to run an experiment forcing the ocean only with the first curl EOF shown in Fig. 15 (experiment ERAEOF1 in Table 1). Fig. 16 presents the first and second amplitude time series (accounting for 70% of the total variance) for the interface displacement and Fig. 17 the corresponding spatial structures. The time series clearly present seasonal and interannual variability with a very similar structure to the amplitude time series of Fig. 10 for the full solution. The spatial structure should be compared with Fig. 11. Evident similarities

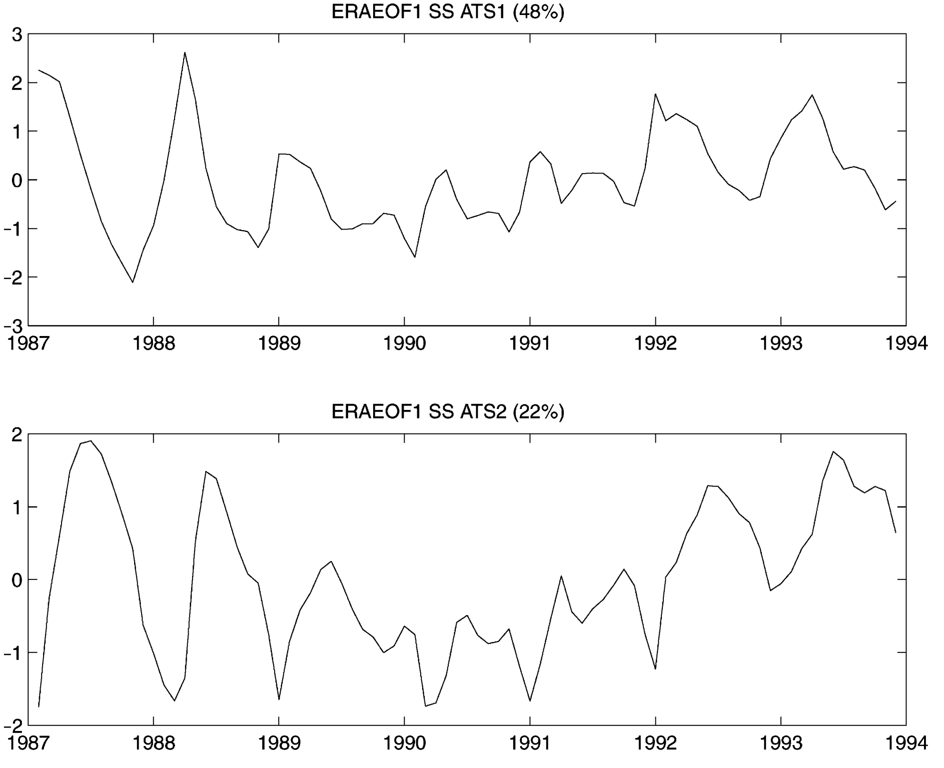

Fig. 16. Amplitude–time series associated with the first (ATS1 upper panel) and the second EOF (ATS2 lower panel) for the ERAEOF1 experiment. This experiment is done forcing the model with the first EOF of the wind stress. The anomalies are calculated substracting the steady-state mean (SS). Numbers in parenthesis at the top of the figures indicate the variance accounted for by each EOF.

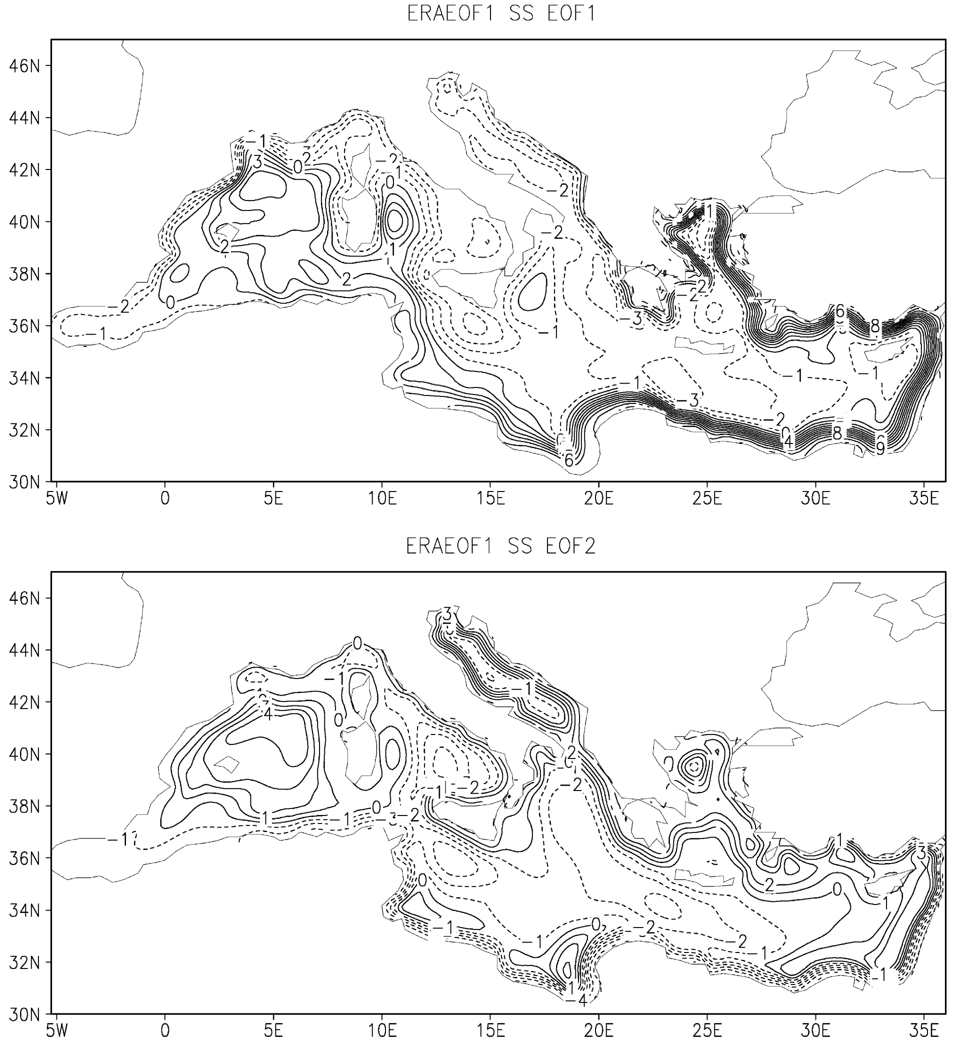

Fig. 17. Spatial structure of the first (upper panel) and second EOF (lower panel) for the ERAEOF1 SS anomalies.

appear from this comparison: Gulf of Lions gyre, northern and eastern Levantine boundary currents, double gyre structure in the Sicilian–Ionian region, double gyre structure in the Tyrrhenian Sea. The large scale Cretan passage–Levantine basin gyre present in Fig. 11 could be compared with the structure present in the second EOF of Fig. 17. Large differences emerge in the regional seas (Adriatic and Aegean) where we expect non-linear viscous effects to be dominant. Thus, we conclude that balance Eq. (8) may hold for the first variability EOF in the curl and ocean response.

The same work has been done for the SC curl anomaly fields in order to compare with the wind-driven interannual circulation anomalies. Fig. 18 presents the first two amplitude time

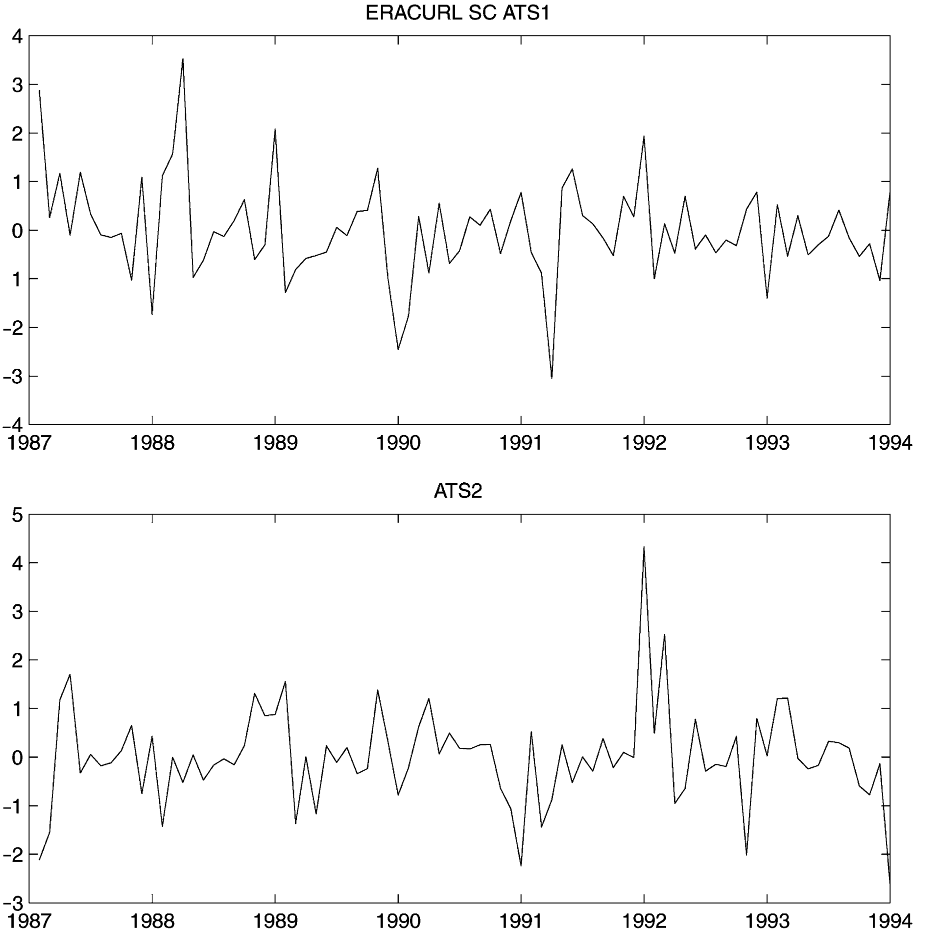

Fig. 18. Amplitude–time series of the first (ATS1 upper panel, 28% of the total variance) and second EOF (ATS2 lower panel, 21% of variance) for ERA wind stress curl SC anomalies.

series. Fig. 19 depicts the curl EOF from SC anomalies: the spatial structures are similar to the curl SS anomaly EOF (Fig. 15) showing that the seasonal and interannual variability has approximately the same spatial structure in the wind stress curl. This explains why the ocean response at interannual and seasonal time scales peaks at the same spatial scales. Computing the correlation coefficients between the first SC curl EOF and the first ocean response SC EOF, we also obtain values ranging between -0.42 and -0.7, excluding the Tyrrhenian, Ionian and the regional seas.

Comparing the SC anomaly EOF of the ocean response (Fig. 13) to the equivalent curl anomalies (Fig. 19) we can deduce that: (1) interannual gyre changes may be caused by corresponding interannual variability changes in wind stress curl. As an example, the dipolar structure in wind stress curl appearing in the western Mediterranean Sea can be visually connected to the dipolar gyre structures of the first EOF of Fig. 13; (2) at the interannual

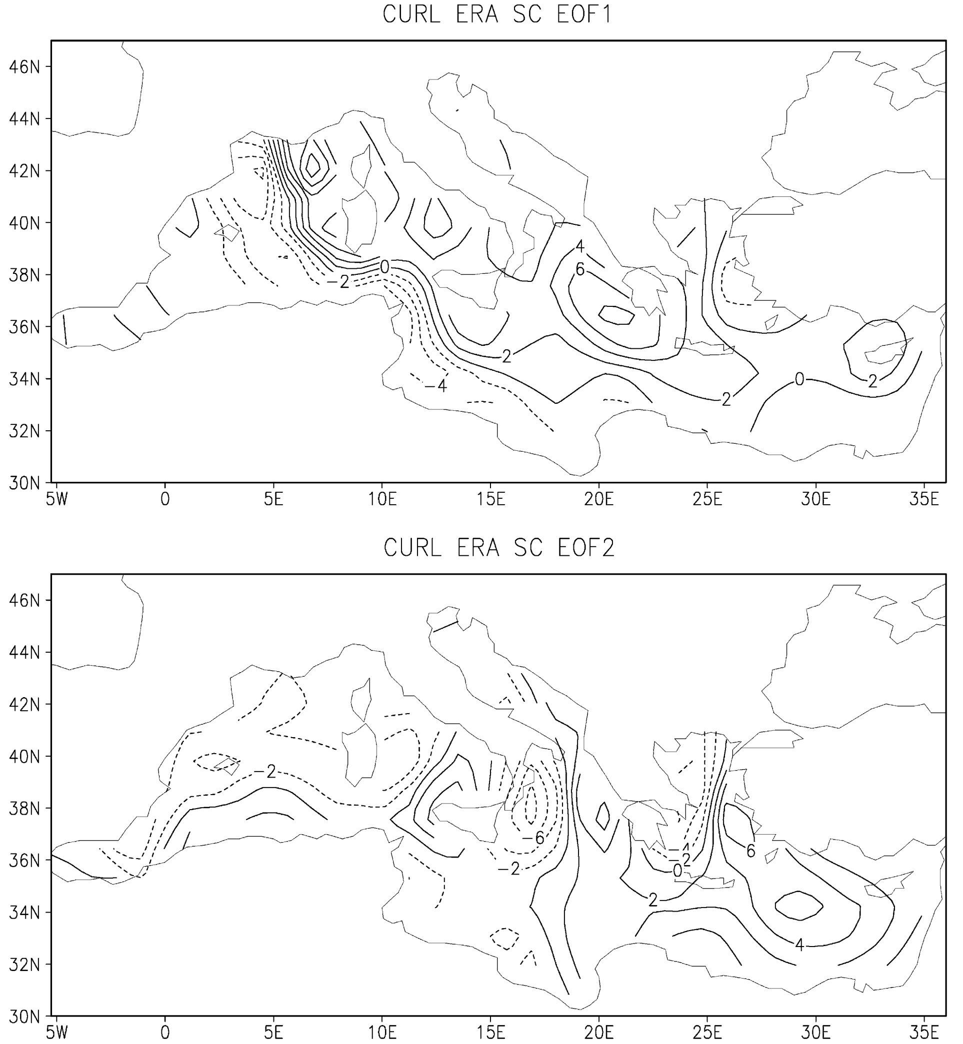

Fig. 19. Spatial structure of the first (upper panel) and second EOF (lower panel) for the ERA wind stress curl SC anomalies.

time scales, the smallest gyre anomalies present in Fig. 13 may not be strictly forced by wind stress curl anomalies especially in the Tyrrhenian and Ionian Seas.

In conclusion, the combined EOF analysis of curl and ocean response points out that in the Mediterranean Sea a time-dependent Sverdrup balance modified by non-linearity and viscosity in boundary layers is achieved. The ocean circulation variability at seasonal and interannual time scales can be explained by changes in wind stress curl vorticity input. However, at interannual time scales, the circulation presents small spatial structures that cannot be explained only by the interannual forcing but involve the internal non-linear response and the memory effects of the circulation.

6. Process studies

6.1. Effect of intensity and spatial variability of the wind forcing

A simulation was carried out by forcing with a double intensity ERA wind stress in order to evaluate qualitatively the impact of known uncertainties in the strength of the atmospheric forcing. A factor of 2 in wind stress intensity corresponds to a change in wind magnitude of approximately 1.4, a value suggested by Cavaleri and Bertotti (1997) to be necessary if realistic wave amplitude was to be reached in the Adriatic Sea. The upper panel of Fig. 20 is

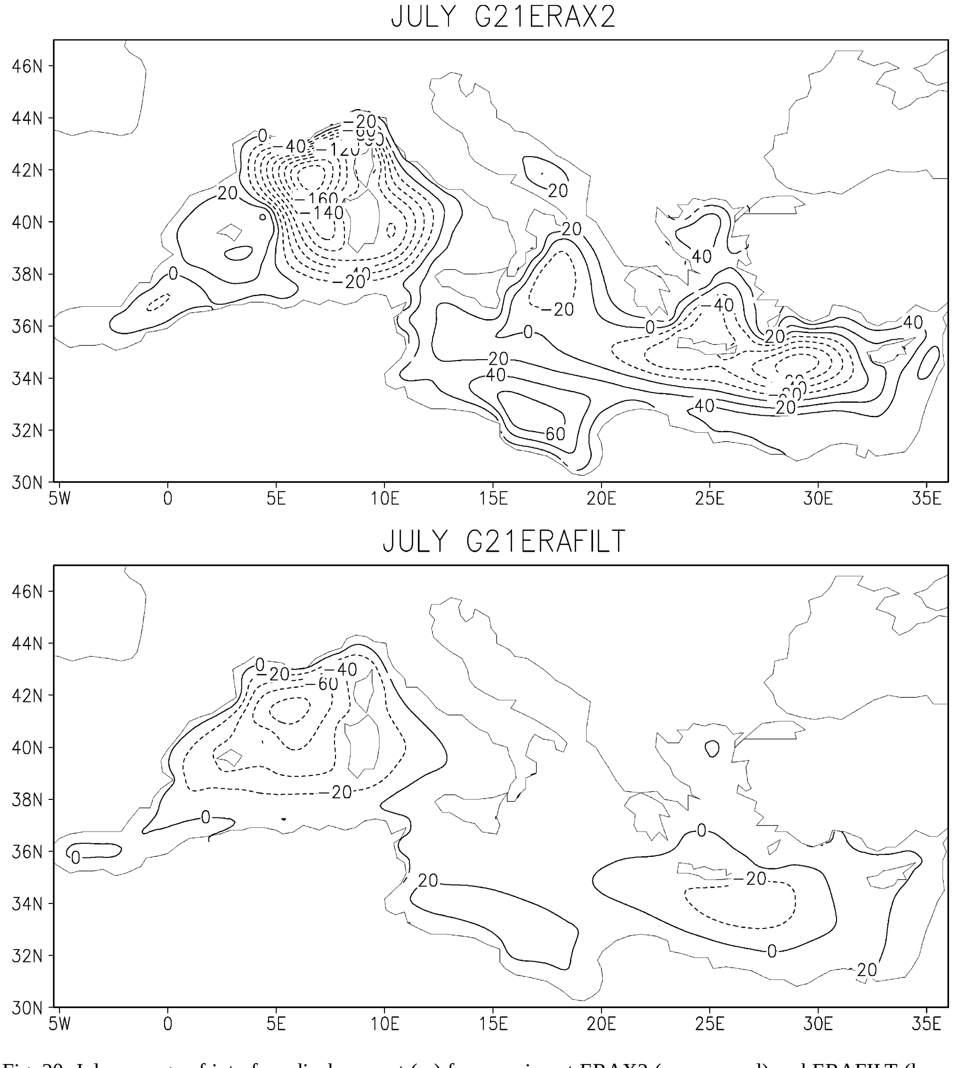

Fig. 20. July average of interface displacement (m) for experiment ERAX2 (upper panel) and ERAFILT (lower panel).

the climatology for July for the interannual simulation ERAX2 (see Table 1). Comparing this circulation with the one in Fig. 9 it seems that the intensity is important for the appearance of the anticyclones in the Balearic Sea, the Tyrrhenian Sea, the Gulf of Syrte and in the Levantine basin boundary current system.

ERA winds stress were then smoothed with a Shapiro filtering procedure (second-order, 100 iterations) in order to evaluate the impact of horizontal spatial structures in the curl. The circulation obtained with this experiment (ERAFILT, see Table 1) is represented in the lower panel of Fig. 20 for the climatological July. The circulation structure is now different from Fig. 9. The sub-basin scale gyres are almost absent except for the Gulf of Lions gyre. This confirms that the spatial structure and intensity of the wind stress curl drives the sub-basin gyres in the basin.

6.2. β-Effect

This simulation is done to verify the effect of the variation of the Coriolis parameter with latitude. Coriolis force is associated with low-frequency Rossby waves that propagate westward in the northern hemisphere. The simulation is done with the COADS wind stress data set, simply setting $\beta = 0$. Fig. 21 represents the climatology of July for the original interannual simulation and the process study experiment COADSNOBETA (see Table 1). Overall the circulation structures moved eastward when considering no β-effect. The anticyclonic system in the southeastern Levantine basin has shrunk down considerably, the anticyclonic gyre in the Gulf of Syrte has amplified and invaded the Ionian and the anticyclonic gyre of the Balearic Sea re-appears. Rossby wave mechanisms are then responsible for the westward displacement of anticyclonic gyres, and their disappearance when they are close to a boundary, as in the case of the Balearic Sea, or appearance as in the case of the southeastern Levantine anticyclonic system.

6.3. Coastal propagation of Kelvin-type waves signals

We analyze the propagation of the waves that follow the coast in a similar way as Milliff and Mc Williams (1994). They showed that, in a square box, Kelvin waves may be excited to travel around the coastlines and at eastern side of the box they may generate Rossby waves which propagate into the interior. We would like to detect this coastal signal due to the wind forcing used in our simulations. The sea surface height values at the coastal grid points are displayed as a function of time in a Hovmoller-type diagram in Fig. 22 for the simulation ERA. Waves traveling with the coast to the right are evident from the slanting of the contours in the anticlockwise direction with respect to the plot axes.

The largest amplitude feature is the one situated between points ‘2’ and ‘15’ (corresponding to the eastern basin perimeter including the Adriatic Sea). This signal represents a coastal wave that propagates counter-clockwise. This Kelvin-type wave has a strong amplitude in 87, 88 and 92 corresponding to maxima in wind stress amplitude (see Fig. 5), and completes eastern basin circumvolution in approximately 7 months, starting from the winter time, corresponding to a phase velocity of about 1 m/s. This velocity is in good agreement with the internal gravity waves velocity computed from the model parameters.

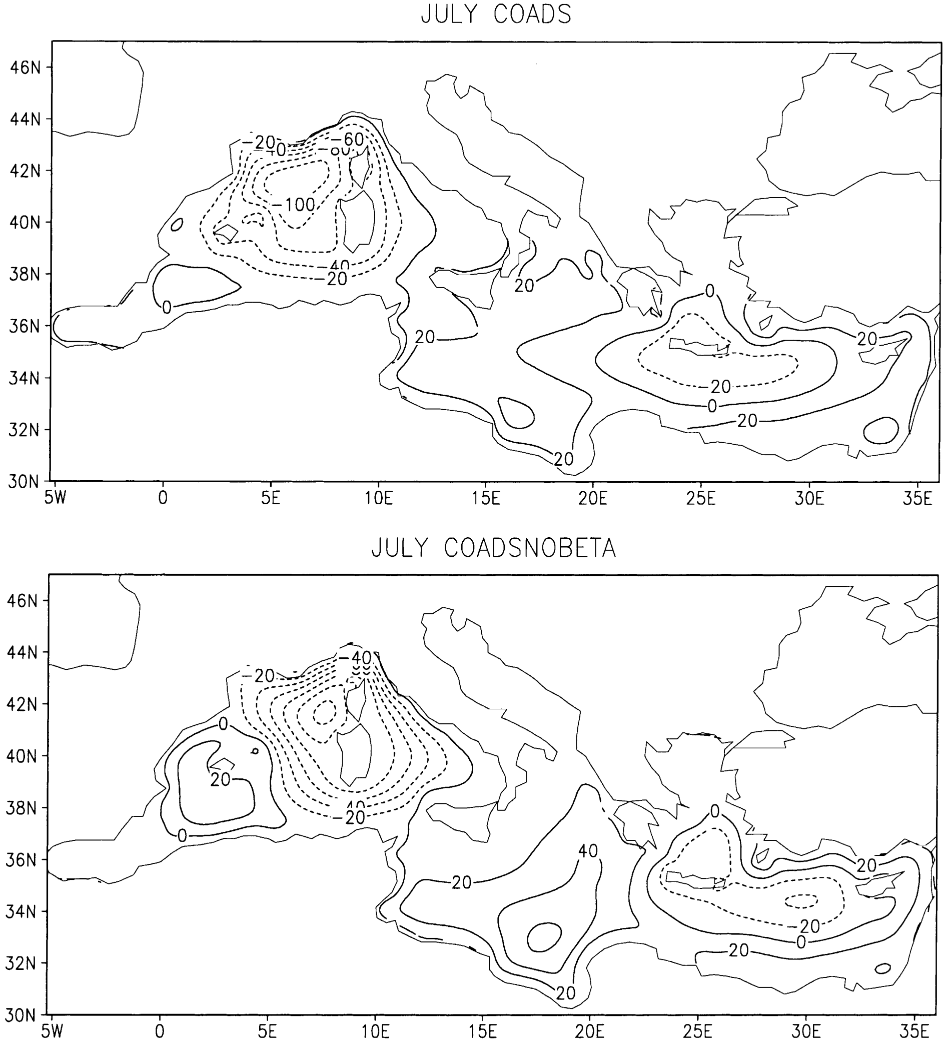

Fig. 21. July average of interface displacement (m) for experiment COADS (upper panel) and COADSNOBETA (lower panel).

A second feature appears along the western basin contour (from points ‘17’ to ‘2’, the Tyrrhenian Sea is not included), and the loop is done in 4 months starting from the summer time. Part of this signal seems to propagates into the eastern basin (the signal goes further than ‘2’) while another part remains in the western basin. In the western basin, the coastal wave does not seem to hug the Tyrrhenian Sea coastline, but probably propagates in the center of this sub-basin (Herbaut et al., 1998).

Finally a third signal in summer time is evident between points ‘8’ and ‘10’, corresponding to the Aegean Sea area. A coastal wave train runs around the Aegean perimeter probably

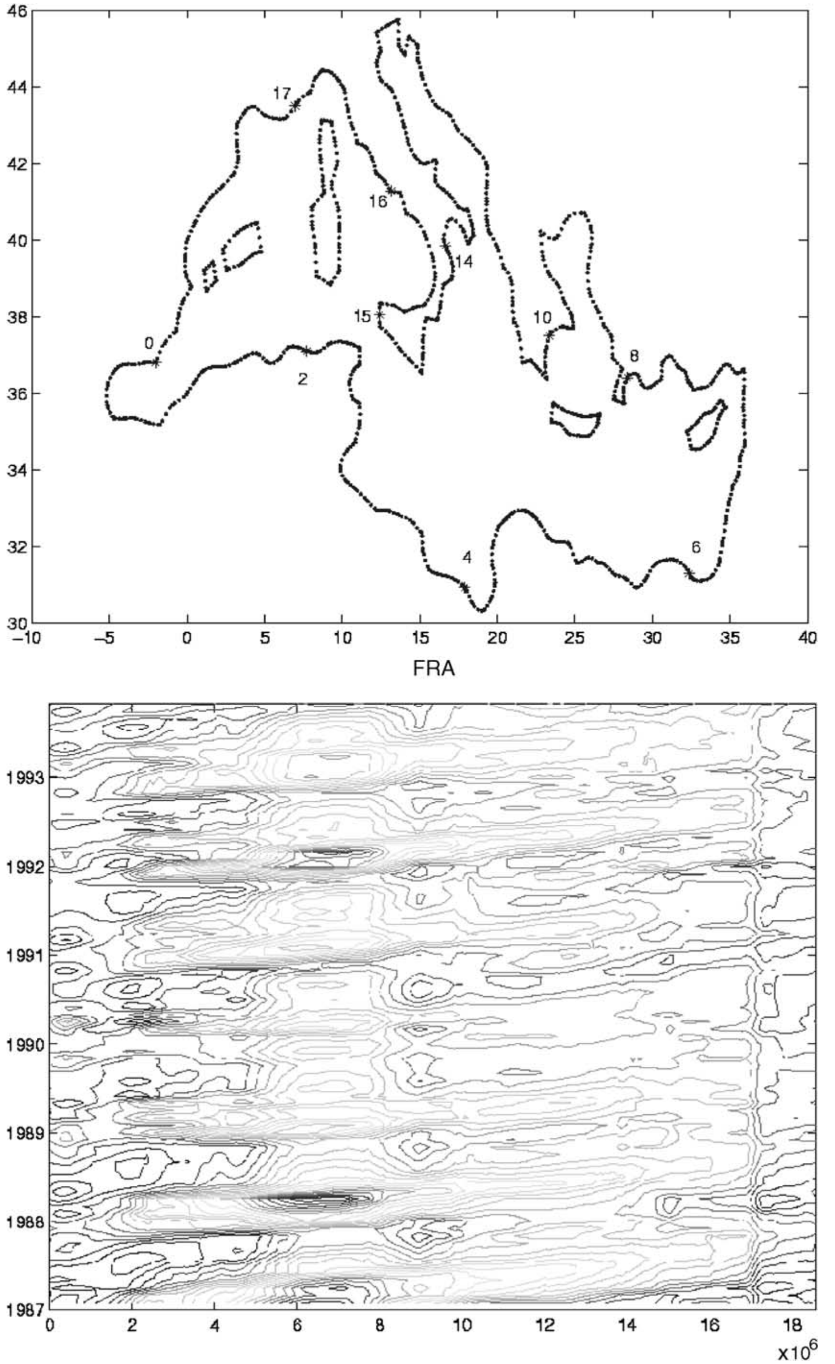

Fig. 22. Upper panel: numbers indicate the points along the boundary that are used in the lower panel to indicate the position along the coast. Lower panel: interface displacement time history (ordinates) as a function of years and point along the boundary for experiment ERA.

excited by the arrival of other coastal signals from the northern Levantine coasts, diffracted by the edges at the eastern entrance of the regional sea.

7. Conclusions

A new implementation of a high accuracy, reduced gravity numerical model has been presented, to study the wind-driven response in the Mediterranean Sea. The study was motivated by the observational evidence of large-scale gyre variability at both seasonal and interannual time scales presumably connected to atmospheric wind forcing variability.

Important results concern the structure of the seasonal and interannual variability of the general circulation. Firstly, we found that the climatological structure of the circulation contains gyres at the sub-basin scale and boundary currents. The permanent gyres are the Gulf of Lions and Rhodes cyclonic gyres and the Gulf of Syrte anticyclone. Smaller spatial scales variability occur at different amplitudes in the remaining sub-basins. The Lions and Rhodes gyres are closed at their northern borders by intense boundary current structures that have large steady state and seasonal fluctuations, respectively for the Lions and Rhodes gyres. The seasonal cycle has the maximum amplitude in the Levantine basin where boundary currents develop in narrow inertial-viscous boundary layers (about 30–50 km in width). The boundary currents may weaken during summer and reconstitute during winter months. Thus, the strength of the boundary current system in the Levantine basin is shown to be an important indicator of seasonal and interannual changes. Furthermore, it has been shown that seasonal and interannual variability spatial structures can be related to wind stress curl anomalies even if at interannual time scales the balance is highly non-linear. A time-dependent Sverdrup balance with inertial-viscous boundary layers dominates the seasonal variability components of the circulation.

Secondly, it was found that interannual and seasonal time scales are coupled and that an important part of the interannual variability of the simulations is contained in the change in amplitude and phase of the seasonal cycle in the 7 years study period. The larger interannual anomalies are connected with the period of smaller seasonal cycle amplitude (1989–1991) and correspond to a strengthening of the western basin cyclonic circulation and weakening of the eastern basin cyclonic flow field.

Energetic coastally trapped wave signals are shown to exist all along the perimeter of the basin, taking about 1 year to circle the entire sea. This corresponds to an internal gravity wave speed of 1 m/s in agreement with our choice of model parameters. These waves are excited by the wind forcing and show large amplitude fluctuations connected to the strength of the driving mechanisms.

Finally it is worth pointing out the possible implications of the seasonal and interannual variability of the gyres and boundary currents. It is well known now that the open ocean oligotrophic character of the Mediterranean Sea is linked to the nutrient supply in cylonic/anticyclonic sub-basin gyres (Crise et al., 1998, 1999). The interannual and seasonal weakening/strengthening of the general circulation gyres for several years may have important consequences for the primary productivity of the sea. These effects should be considered in future studies of the ecosystem dynamics in the Mediterranean Sea.

Acknowledgements

This work was supported by the EU-MAST (contract MAS2-CT94-5017), MATER-MTP (contract MAS3-CT96-0051) and MFSPP (contract MAS3-CT96-0171). All the simulations were run on the CRAY-T3E at CINECA, Bologna, Italy. Development of the Spectral Finite Element Model at Rutgers University is supported by the Office of Naval Research (Contract N00014-93-1-0197). This paper is dedicated to Prof. A. Robinson for his 65th anniversary and for his outstanding contribution to mediterranean science.

Appendix A

We want to compute the correlation coefficient between curl of the wind stress and streamfunction for the classical analytical Stommel solution and show that the correlation coefficient depends on the width of the western boundary layer, e.g. the viscosity parameter of the problem. The classical Stommel balance equation is written, following Hendershott (1987):

$$r\nabla^2\psi + \beta\frac{\partial\psi}{\partial x} = -\frac{\tau_0\pi}{\rho_0 D_0 b}\sin\left(\frac{\pi y}{b}\right) \tag{A.1}$$

$$\tau^x = -\tau_0\cos\left(\frac{\pi y}{b}\right) \tag{A.2}$$

valid for a rectangular basin extending between $x = 0, a$ and $y = 0, b$ with $a = 10^4$ km and $b = a$, $\tau_0 = 0.1\,\text{dyn/cm}^2$ is the amplitude of the zonal wind stress, D_0 is the basin depth, chosen to be 300 m, $\beta = 1.5 \times 10^{-13}$/cm/s and $r = 1/86400T0\,\text{s}^{-1}$ the drag coefficient with $T0$ the dumping time scale in days. Here ψ is the geostrophic streamfunction field. Using the scaling $x \to ax$, $y \to by$, $\psi \to \tau_0/\rho_0 D_0\beta\psi$ we obtain the equation:

$$\epsilon_s\nabla^2\psi + \frac{\partial\psi}{\partial x} = -\pi\sin\left(\frac{\pi y}{b}\right) \tag{A.3}$$

where $\epsilon_s = r/\beta a$ is the width of the Stommel viscous boundary layer. The solution is then:

$$\psi = (1 - e^{-x/\epsilon_s} - x)\pi\sin(\pi y) \tag{A.4}$$

If we calculate the correlation between this solution and the right hand side term of Eq. (A.1), e.g. the wind stress curl, we obtain $C = 0.58$ for $T0 = 1$ day and $C = 0.61$ for $T0 = 10$ days. The correlation is then significant but not necessarely high even for the Stommel case because of the asymmetry between western and eastern boundary layers due to β.

References

Cavaleri, L., Bertotti, L., 1997. In serach of the correct wind and wave fields in a minor basin. Monthly Wether Rev. 125, 1964–1975.

Crepon, M., Richez, C., 1982. Transient upwelling generated by two-dimensional atmospheric and variability in the coastline. J. Phys. Oceanogr. 12 (12), 1437–1457.

Crise, A., Crispi, G., Mauri, E., 1998. A seasonal three-dimensional model of the nitrogen cycle in the Mediterranean Sea. Part I. Model implementation and numerical results. J. Marine Syst. 18, 287–312.

Crise, A., Crispi, G., Mauri, E., 1999. A seasonal three-dimensional model of the nitrogen cycle in the Mediterranean Sea. Part II. Verification of the energy constrained trophic model. J. Marine Syst. 20, 357–379.

Curchitser, E.N., Iskandarani, M., Haidvogel, D., 1998. A spectral element solution of the shallow water equations on multiprocessor computers. J. Atmos. Oceanogr. Technol. 15, 510–521.

Curchitser, E.N., Haivogel, D., Iskandarani, M., 1999. On the transient adjustment of a mid-latitutde Abyssal ocean basin with realistic geometry: the constant depth limit. Dyn. Atmos. Oceans 29 (2/4), 147.

Curchitser, E.N., Haivogel, D., Iskandarani, M., 2001. On the transient adjustment of a mid-latitude Abyssal ocean basin with realistic geometry and bathymetry. J. Phys. Oceanogr., in press.

Demirov, E., Pinardi, N., 2001. Simulation of the Mediterranean Sea circulation from 1979 to 1993. Part I. The interannual variability. J. Marine Sci., in press.

Emery, W.J., Thomson, R.E., 1997. Data Analysis Methods in Physical Oceanography. Elsevier, New York, USA.

Hecht, A., Pinardi, N., Robinson, A., 1988. Currents, water masses, Eddies and jets in the Mediterranean Levantine basin. J. Phys. Oceanogr. 18, 1320–1353.

Hellerman, S., Rosenstein, M., 1983. Normal monthly wind stress over the world ocean with error estimates. J. Phys. Oceanogr. 13 (7), 1093–1104.

Hendershott, M.C., 1987. Single layer models of the general circulation. In: Abarbanel and Young (Eds.), General circulation of the ocean. Inc. Springer-Verlag, New York.

Herbaut, C., Mortier, L., Crepon, M., 1996. A sensitivity study of the general circulation of the western Mediterranean. Part I. The response to density forcing through the Straits. J. Phys. Oceanogr. 26 (1), 65–84.

Herbaut, C., Codron, C., Crepon, M., 1998. Separation of a coastal current at a strait level: case of Strait of Sicily. J. Phys. Oceanogr. 38, (7).

Horton, C., Clifford, M., Schmitz, J., Kantha, L.H., 1997. A real-time oceanographic nowcast–forecast system for the Mediterranean Sea. J. Geophys. Res. 102 (C11), 25123–25156.

Iskandarani, M., Haidvogel, D., Boyd, J.P., 1995. A staggered spectral element model for the shallow water equations. Int. J. Numer. Meth. Fluids 20 (5), 393–414.

Korres, G., Pinardi, N., Lascaratos, A., 2000a. The ocean response to low frequency interannual atmospheric variability in the Mediterranean Sea. Part I . Sensitivity experiments and energy analysis. J. Climate 13 (4), 705–731.

Korres, G., Pinardi, N., Lascaratos, A., 2000b. The ocean response to low frequency interannual atmospheric variability in the Mediterranean Sea. Part II . Empirical orthogonal functions analysis. J. Climate 13 (4), 732–745.

Levin, J., Iskandarani, M., Haidvogel, D.B., 2000. A non-conforming spectral element ocean model. Int. J. Numer. Meth. Fluids 34 (6), 495–525.

Malanotte-Rizzoli, P., Bergamasco, A., 1989. The wind and thermally-driven circulation of the eastern Mediterranean. Part I. Oceanologica Acta 12 (4), 335–351.

Malanotte-Rizzoli, P., Bergamasco, A., 1991. The circulation of the eastern Mediterranean Sea. Part II. The baroclinic case. Dyn. Atmos. Oceans 15, 355–371.

Malanotte-Rizzoli, P., Manca, B.B., RiberadAlcala, M., Theocharis, A., Bergamasco, A., Bregant, D., Budillon, G., Civitarese, G., Georgopoulos, D., Michelato, A., Sansone, E., Scarazzato, P., Souvermezoglou, E., 1998. A synthesis of the Ionian Sea hydrography circulation and water mass pathways during POEM phase I. Prog. Oceanogr. 39, 153–204.

Milliff, R.F., McWilliams, J., 1994. The evolution of boundary pressure in ocean basin. J. Phys. Ocean 24, 1317–1338.

Millot, C., 1994. Models and data: a synergetic approach in the western Mediterranean Sea. In: Malanotte-Rizzoli, P., Robinson, A.R. (Eds.), Ocean Processes in Climate Dynamics: Global and Mediterranean Examples. Kluwer Academic Publishers, Dordrecht, The Netherlands, 1994, pp. 407–425.

Molcard, A., Pinardi, N., Ansaloni, R., 1998. A Spectral Element Ocean Model on the CRAY-T3E: the interannual variability of the Mediterranean Sea general circulation. Phys. Chem. Earth 23 (5/6), 491–495.

Moskalenko, L.V., 1974. Steady-state wind-driven currents in the eastern half of the Mediterranean Sea. Okianologia 14 (4), 491–494.

Pedlosky, J., 1987. Geophysical Fluid Dynamics. Springer, New-York.

Pierini, S., 1998. Wind-driven fluctuating western boundary currents, J. Phys. Oceanogr. 28 (11), 2185–2198.

Pinardi, N., Navarra, A., 1993. Baroclinic wind adjustement processes in the Mediterranean Sea. Deep-Sea Res. II 40 (6), 1299–1326.

Pinardi, N., Korres, G., Lascaratos, A., Roussenov, V., Stanev, E., 1997. Numerical simulation of the Mediterranean Sea upper ocean circulation. Geophys. Res. Lett. 24 (4), 425–428.

POEM Group, 1992. General circulation of the eastern Mediterranean. Earth-Sci. Rev. 32, 285–309.

Robinson, A.R., Golnaraghi, M., 1993. Circulation and dynamics of the eastern Mediterranean Sea; quasi-synoptic data-driven simulations. Part II. Deep Sea Research. Topical Stud. Oceanogr. 40 (6), 1207–1246.

Robinson, A.R., Golnaraghi, M., Leslie, W.G., Artegiani, A., Hecht A, , Lazzoni, E., Michelato, A., Sansone, E., Theocaris, A., Unluata, U., 1991. Structure and variability of the eastern Mediterranean general circulation. Dyn. Atmos. Oceans 15, 215–240.

Roussenov, V., Stanev, E., Artale, V., Pinardi, N., 1995. A seasonal model of the Mediterranean Sea general circulation. J. Geophys. Res. 100, 13515–13538.

Samuel, S., Haines, K., Josey, S., Myers, P., 1998. Response of the Mediterranean Sea thermohaline circulation to observed changes in the winter wind stress field in the period 1980–1993. J. Geophys. Res. 104, C4, 7771–7784, submitted for publication.

Smith, S.D., 1980. Wind stress and heat flux over the ocean in Gale force winds. J. Phys. Oceanogr. 10, 709–725.

Taylor, M., Tribbia, J., Iskandarani, I., 1997. The spectral element method for the shallow water equations on the sphere. J. Comput. Phys. 130 (1), 92–108.

Wingate, B., Boyd, J.P., 1996. Spectral element methods on triangles for geophysical fluid dynamics problems. In: Proccedings of the Third International Conference on Spectral and High-order Methods. Ilin and Scott, Houston, TX.

Zavatarelli, M., Mellor, G.L., 1995. A numerical study of the Mediterranean Sea circulation. J. Phys. Oceanogr. 46, 8–688.